Journal of Molecular Structure 1368 (2026) 146312

Contents lists available at ScienceDirect

Journal of Molecular Structure

journal homepage: www.elsevier.com/locate/molstr

New thiophene pyrazole hybrid: An efficient synthesis, X-ray analysis, computational and in silico studies

Abdullatif Bin Muhsinah [a], Nabila A. Kheder [b], Ismail A. Elhaty [c,*], Naglaa S. Mahmoud [d], Yahia N. Mabkhot [e,*]

[a] Department of Pharmacognosy, College of Pharmacy, King Khalid University, P.O. Box 960, Abha 61421, Saudi Arabia
[b] Department of Chemistry, Faculty of Science, Cairo University, Giza 12613, Egypt
[c] Department of Nutrition and Dietetics, Faculty of Health Sciences, Istanbul Gelisim University, Istanbul, Turkey
[d] Department of Industrial Pharmacy, College of Pharmaceutical Sciences and Drug Manufacturing, Misr University for Science and Technology, Giza, P.O. 12566, Egypt
[e] Department of Pharmaceutical Chemistry, College of Pharmacy, King Khalid University, Abha 61441, Saudi Arabia

ARTICLE INFO

Keywords:
Thiophene
Pyrazole
X-ray analysis
Computational study
Drug likeness

ABSTRACT

A one-pot, three-component synthesis of ethyl 5-(3-ethoxy-3-oxopropanoyl)-4-phenyl-2-(phenylamino)thiophene-3-carboxylate (**7**) was reported. Its reaction with DMF-DMA and phenylhydrazine produced a thiophene pyrazole hybrid **8**. The chemical structures of the synthesized compounds were confirmed using spectral (IR, NMR, MS) and elemental analysis. Additionally, the 3D structure of compound **8** was confirmed by single-crystal X-ray diffraction.

The crystallographic study revealed that compound **8** is mainly stabilized by weak C—H•••O and C—H•••N contacts together with dispersive interactions. Hirshfeld surface analysis revealed that crystal packing is dominated by H•••H (57.9%), C•••H (18.6%), and O•••H (10.6%) interactions. DFT calculations for compounds **7** and **8** support experimental interpretation. MEP surface showed that carbonyl oxygen atoms are the richest regions, while FMO analysis indicated moderate HOMO/LUMO gaps (4.032 for **7** and 4.125 eV for **8**), consistent with a stable and polarizable conjugated system. NBO and Mulliken charge analyses are consistent with MEP results. *In silico* ADME prediction was performed to evaluate the physicochemical and pharmacokinetic properties of the synthesized compounds. Molecular docking studies were conducted against the EGFR protein (PDB ID: 5UGB) to investigate their potential as anticancer leads. The results revealed that compound **7** exhibited the most favorable predicted binding activity, while both compounds demonstrated binding patterns and affinities comparable to the reference drug.

1. Introduction

Thiophene-containing compounds exhibit a wide range of pharmacological activities, including antidepressant [1], antimicrobial [2], anti-inflammatory [3], analgesic [4], and anticonvulsant [5] properties. In addition, the anticancer profile of thiophene derivatives has been extensively explored [6] [Fig. 1].

Pyrazole derivatives exhibit various pharmacological activities, including anticancer [7], antimicrobial [8], antimalarial [9], anti-inflammatory [10], anticonvulsant [11], and antiviral [12] properties. Crizotinib, Pralsetinib, Avapritinib, and Asciminib are some examples of marketed anticancer drugs containing a pyrazole nucleus [13] (Fig. 2).

Encouraged by the extensive applications of thiophene and pyrazole derivatives and as an extension of our study on possible approaches to novel heterocyclic compounds of expected biological activity [14–20], herein we report an efficient one-pot-three-component synthetic method for the synthesis of a new thiophene and thiophene pyrazole hybrid. Its structure was characterized using several spectroscopic techniques and single crystal x-ray diffractions. Hirshfeld surface and computational analyses were used to study the structure properties. *In silico* ADME prediction and molecular docking studies have been used for evaluating physicochemical and pharmacokinetic properties and predicting potential biological activity of the newly synthesized scaffolds.

* Corresponding authors.
E-mail addresses: iaeismail@gelisim.edu.tr (I.A. Elhaty), alzooba8@gmail.com (Y.N. Mabkhot).

https://doi.org/10.1016/j.molstruc.2026.146312
Received 4 February 2026; Received in revised form 8 April 2026; Accepted 18 April 2026
Available online 19 April 2026

2. Materials and methods

2.1. Chemistry

2.1.1. General remarks

All reagents and solvents were bought from usual commercial sources, including Sigma-Aldrich (St. Louis, MO, USA), and used without further purification. The Supplementary file contains details of all analytical and spectroscopic instruments employed to characterize thiophene-based heterocycles **7** and **8**.

2.1.2. Synthesis of ethyl 5-(3-ethoxy-3-oxopropanoyl)-4-phenyl-2-(phenylamino)thiophene-3-carboxylate (7)

A mixture of ethyl benzoylacetate (**1**) (1.92 g, 10 mmol) and anhydrous K_2CO_3 (1.4 g) in DMF (10 mL) was stirred at room temperature for 10 min. Then, phenyl isothiocyanate (1.35 mL, 10 mmol) was added, and stirring continued for 1 hour. To the reaction mixture, ethyl 4-chloro-3-oxobutanoate (1.64 mL, 10 mmol) was added, and the mixture was stirred for 12 h. Finally, the reaction mixture was poured into an ice-water mixture and neutralized with a diluted solution of HCl. The solid product was filtered, washed with water, and dried. Recrystallization from ethanol produced yellow crystals of compound **7** in 78% yield; mp. 95 °C; IR (KBr, cm^{-1}) νmax = 2972 (aliphatic CH), 1559 (C = O) cm^{-1}; ^{1}H NMR (400 MHz, DMSO-d_6): δ 0.68 (t, 3H, J = 5.7 Hz, CH_3CH_2O), 1.09 (t, 3H, J = 5.7 Hz, CH_3CH_2O), 2.96 (s, 2H, CH_2—C = O), 3.86 (q, 2H, J = 5.7 Hz, OCH_2CH_3), 3.94 (q, 2H, J = 5.7 Hz, OCH_2CH_3), 7.28–7.50 (m, 10H, ArH), 10.51 (s, 1H, NH); ^{13}C NMR (100 MHz, DMSO-d_6): δ 13.5 (CH_3CH_2O), 14.3 (CH_3CH_2O), 46.3 (CH_2—C = O), 60.1 (CH_3CH_2O), 61.0 (CH_3CH_2O), 122.0, 126.0, 128.4, 128.6, 129.0, 130.3 (6 aromatic CH carbons), 110.3, 122.9, 136.6, 140.0, 148.3, 164.5 (6 quaternary aromatic carbons), 165.3 (C = O), 167.5 (C = O), 185.4 (C = O). MS (ESI-QTOF): calcd. for $[M + H]^+$ m/z = 438.14; found 438.1028. Anal Calcd. for $C_{24}H_{23}NO_5S$ (437.51): C, 65.89; H, 5.30; N, 3.20. Found: C, 65.72; H, 5.12; N, 3.33. SMILES: O = C(CC(OCC)=O)C1=C(C2=CC=CC=C2)C(C(OCC)=O)=C(NC3=CC=CC=C3)S1.

2.1.3. Synthesis of ethyl 5-(4-(ethoxycarbonyl)-3-phenyl-5-(phenylamino) thiophen-2-yl)-1-phenyl-1H-pyrazole-4-carboxylate (8)

A mixture of thiophene derivative **7** (0.87 g, 2 mmol) and DMF-DMA (0.95 g, 8 mmol) was heated at 120 °C for 30 min. Then, the crude residue was used directly in the next reaction without further purification. A mixture of crude residue and $PhNHNH_2$ (0.22 g, 2 mmol) in ethanol (10 ml) was heated under reflux for 4 h. The solid that precipitated was filtered, dried, and recrystallized using ethanol to afford

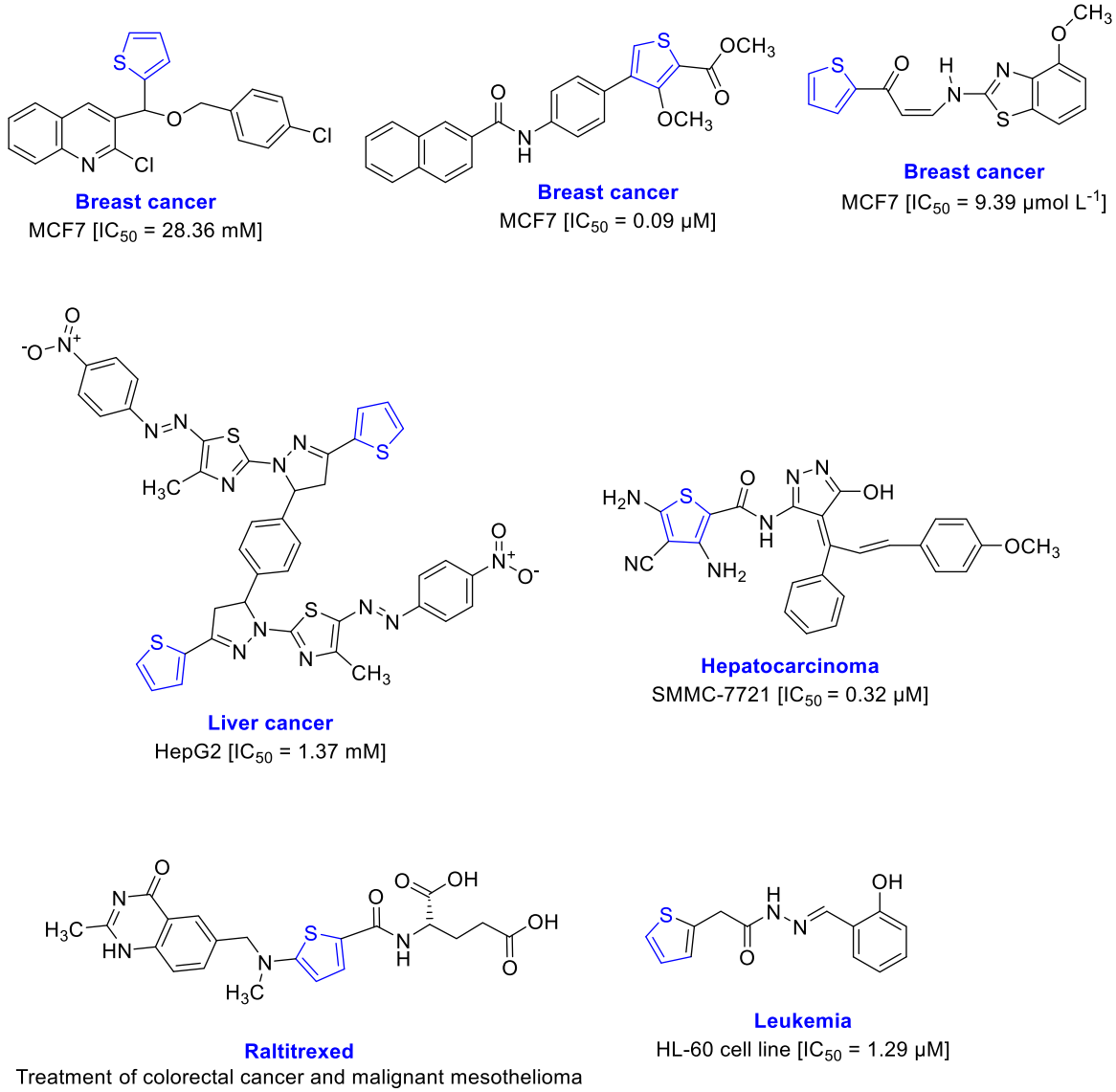

Fig. 1. Anticancer medications contain a thiophene moiety.

yellow crystals of compound **8** in 85% yield, mp. 170 °C IR (KBr, cm^{-1}) ν_{max} = 1719, 1663 (2C═O) cm^{-1}; ^{1}H NMR (400 MHz, DMSO-d_6): δ 0.73 (t, 3H, CH_3CH_2O), 1.24 (t, 3H, CH_3CH_2O), 3.91 (q, 2H, OCH_2CH_3), 4.24 (q, 2H, OCH_2CH_3), 6.52–8.07 (m, 16H, ArH), 10.05 (s, 1H, NH); ^{13}C NMR (100 MHz, DMSO-d_6): δ 13.7 (CH_3CH_2O), 14.6 (CH_3CH_2O), 60.0 (CH_3CH_2O), 60.4 (CH_3CH_2O), 119.9, 124.4, 124.6, 127.3, 127.5, 128.5, 128.9, 129.4, 130.2, 142.1 (10 aromatic CH carbons), 107.3, 108.0, 117.3, 135.8, 137.3, 138.9, 141.0, 160.4 (8 quaternary aromatic carbons), 162.1 (C = O), 165.1 (C = O); MS (ESI-QTOF): calcd. for $[M + H]^+$ m/z = 538.18; found 538.1370. Anal Calcd. For $C_{31}H_{27}N_3O4S$ (537.63): C, 69.26; H, 5.06; N, 7.82. Found. C, 69.18; H, 5.21; N, 7.69. SMILES: O = C(C1=C(C2=C(C3=CC═CC═C3)C(C(OCC)=O)=C(NC4=CC═CC═C4)S2)N(C5=CC═CC═C5)N = C1)OCC.

2.2. X-ray crystallography

A pale-yellow block-shaped crystal of compound **8** was prepared by slow evaporation of its ethanolic solution at room temperature. X-ray diffraction data were collected at 293 K on an Rigaku Oxford Diffraction SuperNova diffractometer equipped with a HyPix3000 detector and Mo Kα radiation (λ = 0.71073). The cell unit parameters and intensity data were determined using CrysAlis PRO software package. The structure was solved by direct methods using SHELXT and refined by full-matrix least-squares on F^2 using SHELXL [21,22]. All non-hydrogen atoms were refined anisotropically. Hydrogen atoms were placed in calculated positions and refined using a riding model. Molecular graphics were generated using Mercury 4.2.0 [23]. The Crystallographic data for compound **8** has been deposited with the Cambridge Crystallographic Data Centre (CCDC) under deposition number 2519,126. The data can be obtained free of charge from www.ccdc.cam.ac.uk/data_request/cif.

Several attempts under various crystallization conditions were made to obtain single crystal of compound **7** suitable for X-ray diffraction were unsuccessful. Compound 7 consistently formed a microcrystalline powder, therefore XRD are reported only for compound **8**.

2.3. Computational analysis

2.3.1. Hirshfeld surface analysis

Hirshfeld surface analysis [24] was performed for the compound **8** crystal to visualize the intermolecular interactions in this compound based on its crystallographic information file (CIF) and using the CrystalExplorer 17.5 program [25]. In addition, two-dimensional fingerprint plots [26] were generated using the same program.

2.3.2. Frontier molecular orbital (FMO) analysis and global reactivity descriptors

Frontier Molecular Orbital calculations were carried out on the optimized structure of compounds **7** and **8** (Fig. 3), which optimized using density functional theory (DFT) with the B3LYP method and basis sets of 6–311++G(d,p) under neutral conditions [27]. The atom

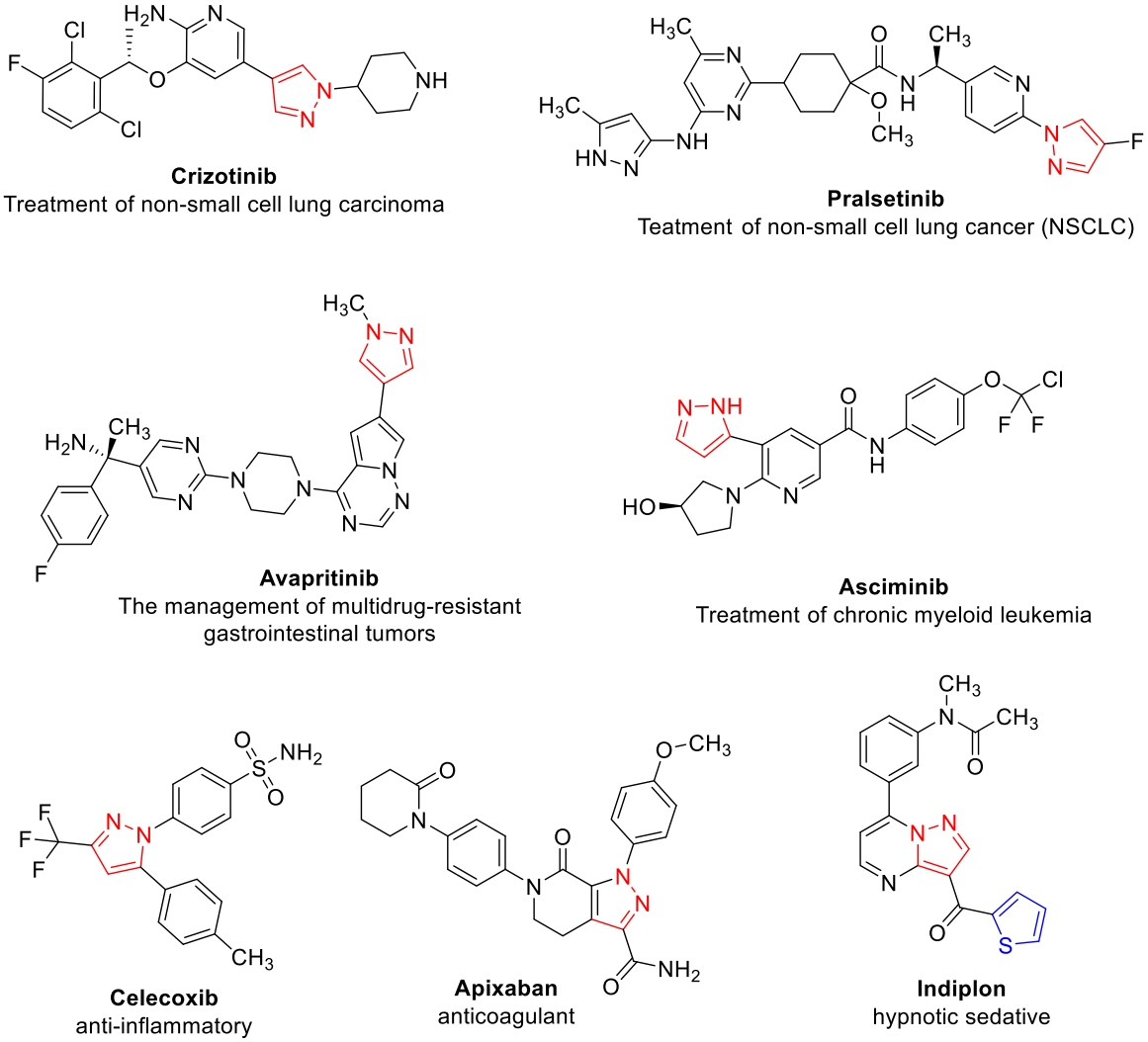

Fig. 2. Chemical structures of pyrazole-based commercial drugs.

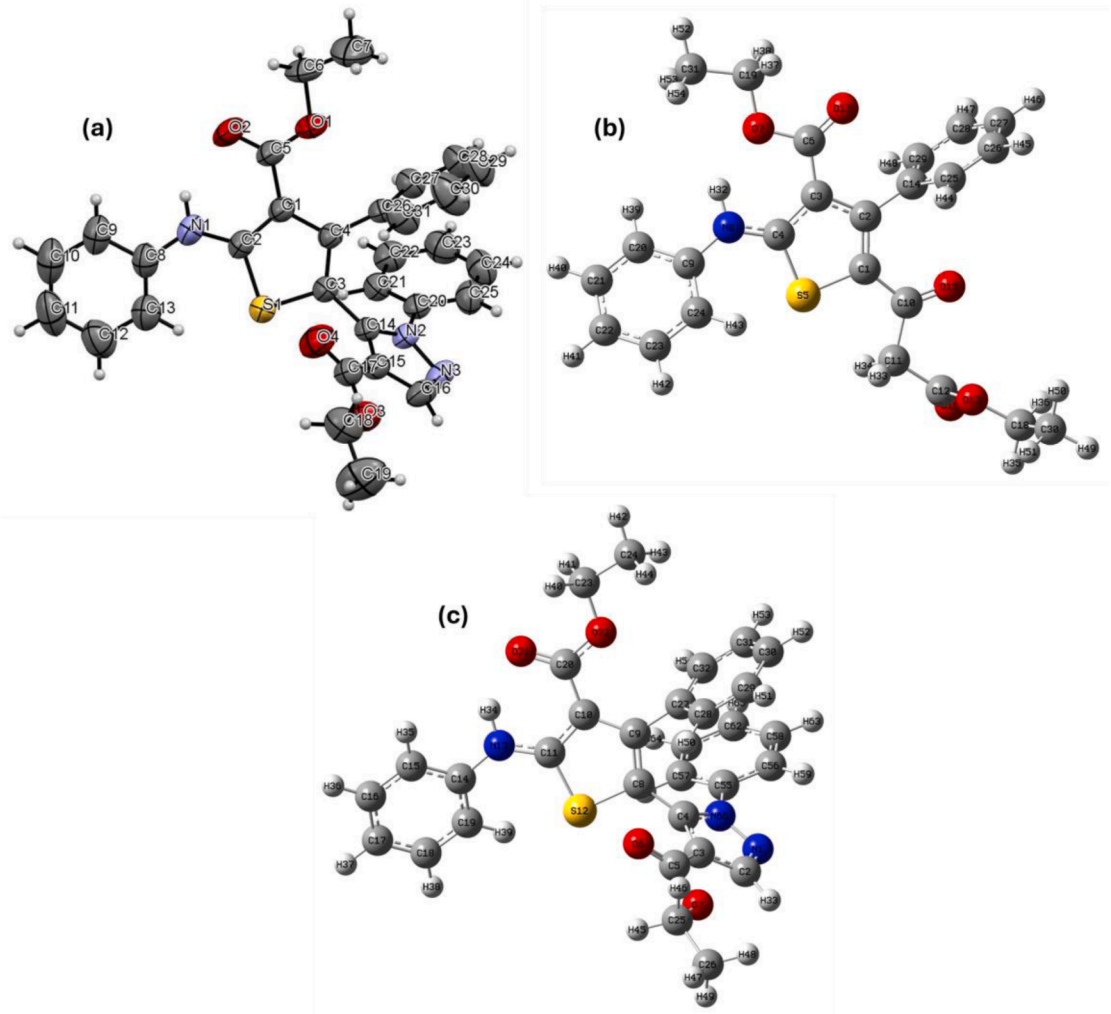

Fig. 3. X-ray structure of compound **8** (a) and the optimized structure of compounds **7** (b) and **8** (c).

numbering used in DFT and NBO follows the Gaussian ordering and is different from the crystallographic labels as indicated in Fig. 3 and **Table S9**. The Highest Occupied Molecular Orbital (HOMO) and Lowest Unoccupied Molecular Orbital (LUMO) were visualized using Gauss-View 5.0. FMOs provide an important insight into the chemical reactivity, active sites, and kinetic stability of the target molecule. The energy difference (ΔE) between HOMO and LUMO was calculated. It indicates the reactivity of a molecule where the large gap indicates a chemically stable molecule [28].

In addition, the electronic stability, charge transfer characteristics, and potential interaction profiles for compounds **7** and **8** were further studied by computing the global reactivity descriptors using the frontier molecular orbital energies. The calculated parameters include ionization potential (I), electron affinity (A), electronegativity (χ), chemical potential (μ), hardness (η), and softness (S).

2.3.3. *Molecular electrostatic potential (MEP) mapping*

The optimized structures of compounds **7** and **8** were employed to study the charge distribution within these compounds and their molecular reactivity regarding electrophilic and nucleophilic attacks, via the molecular electrostatic potential (MEP) surface analysis. The color code of MEP surface indicates susceptible sites within the molecule to electrophilic (red) and nucleophilic (blue) attacks [29]. In addition, these colored-coded regions may help in predicting available non-covalent interactions.

2.3.4. *NBO charge and Mulliken population analysis*

The calculation of atomic charges within the optimized structures were performed using NBO atomic charges and Mulliken charge analysis according to the above-mentioned DFT level. Both analyses are efficient and simple methods commonly used to provide information about the distribution of electronic charges across a molecule's atoms.

2.4. *In silico physicochemical, pharmacokinetic, and toxicological assessments*

Physicochemical properties and pharmacokinetic parameters of the synthesized compounds were predicted using the SwissADME web server (https://www.swissadme.ch/).

2.5. *Docking*

The optimized ligand structures of compounds **7** and **8** were obtained from prior DFT calculations and X-ray, respectively. The crystal structure of the epidermal growth factor receptor EGFR (PDB ID: 5UGB) was retrieved from the Protein Data Bank and prepared by the standard Autodock tools protocol. Molecular docking was performed using AutoDock Vina, targeting the native ligand binding pocket [30]. Protein–ligand interactions were visualized using Discovery Studio Client (free version) for 2D images and UCSF Chimera for 3D images.

2.6. In silico evaluation of toxicity and drug likeness

A preliminary *in silico* evaluation of the toxicity risk flags and the basic drug likeness descriptors for compounds **7** and **8** were conducted using the OSIRIS Property Explorer [31]. In this assessment, OSIRIS measures the closeness of the compound's properties to those of known therapeutic agents based on the compound's lipophilicity (log P), solubility (log S), molecular weight, and toxicity risks, including mutagenicity, tumorigenicity, irritating effects, and reproductive effects.

3. Results and discussion

3.1. Synthesis and characterization

The reaction of ethyl benzoylacetate (**1**) with PhNCS (**2**) in a K_2CO_3/DMF mixture produced potassium salt **3**, which, upon addition of ethyl 4-chloro-3-oxobutanoate, yielded a thiophene derivative **7** (Scheme 1). Its chemical structure was determined based on spectral data. For example, the ^{1}H NMR spectrum showed two triplet signals at δ 0.68 and 1.09, corresponding to two CH_3 protons, and two quartet signals at δ 3.86 and 3.94, due to two CH_2 protons. It also exhibited two singlet signals at δ 2.96 and 10.51, which are attributed to CH_2 and NH protons, respectively, along with an aromatic multiplet in the region of 7.28–7.50 ppm.

^{13}C NMR spectrum data confirmed the assigned structure and gave 20 signals as expected (**Figs. S2**, SI File). The ^{13}C-DEPT-135 NMR spectrum (**Fig. S3**) showed the presence of eight positive signals at δ 13.5, 14.3, 122.0, 126.0, 128.4, 128.6, 129.0, 130.3 due to two CH_3 and six CH carbons. Additionally, it displayed three negative signals at δ 46.34, 60.12, and 60.96 ppm, which were attributed to three CH_2 carbons.

Connecting thiophene with a pyrazole moiety enhances the biological activities of the resulting hybrid structure. The synthesis of thiophene pyrazole hybrid **8** could be performed using a thiophene derivative **7** as a starting material.

In thiophene **7**, the activating effect of the two carbonyl groups on the active methylene function makes it susceptible to the condensation reaction with dimethylformamide dimethyl acetal (DMF-DMA), forming the intermediate **9**, which, upon reaction with phenyl hydrazine, yields the target compound **8** (Scheme 2).

Spectroscopic methods (IR, NMR, MS) confirmed the structure of thiophene **8**.

Its ^{1}H NMR spectrum showed four characteristic signals at δ 0.73, 1.24, 3.91, and 4.24 due to the protons of two ester groups, along with a singlet at δ 10.05, which was attributed to the NH proton.

The 13C-DEPT-135 NMR spectrum of **8** [**Fig. S8**, SI file] showed twelve positive signals at δ 13.7, 14.6, 119.9, 124.4, 124.6, 127.3, 127.5, 128.54 128.9, 129.4, 130.2, 142.1, attributed to two CH_3 and ten CH carbons. It also displayed two methylene carbons as negative signals at δ 60.0 and 60.4.

Additionally, the exact mass measured by HRMS was *m/z* 538.1370, consistent with the calculated value of *m/z* 538.18 $[M + H]^+$. The 3D structure of compound **8** was also confirmed by single-crystal X-ray diffraction.

To explain the synthesis of **8**, we assumed that the reaction began with the condensation of thiophene **7** with DMF-DMA to form intermediate **9**, which then reacted with phenyl hydrazine to produce **11** (Scheme 2). Cyclization of **11** proceeds via loss of one water molecule (route a) to afford the thiophene-pyrazole hybrid **8**. The other possible products, **12** and **13**, outlined in Scheme 2, were excluded based on the spectral information (**Figs. S4** to **S8**, SI file).

3.2. X-Ray structure description

The molecular structure of compound **8** was approved by single crystal X-ray diffraction analysis (Fig. 3a). The detailed crystallographic data of compound **8** are shown in Table 1. The structure was crystallized with one molecule in the asymmetric unit in the triclinic crystal system space group P −1 with Z = 2 and a unit-cell volume = 1426.63(17) Å^3.

The geometry of the thiophene ring (S1/C1-C4) is consistent with reported geometry, with S1-C2 and S1-C3 distances of 1.7251(19) and 1.7301(18) Å, respectively, and C3-S1-C2 angle of 91.14(9)° as shown in Table 2. In addition, the two carbonyl groups are of typical lengths, where O2=C5 = 1.213(2) Å and O4=C17 = 1.197(2) Å. Moreover, the N—N linkage length (N2-N3 = 1.3645(19) Å indicates a partial double-bond character, consistent with the conjugation through the N2-N3-C16

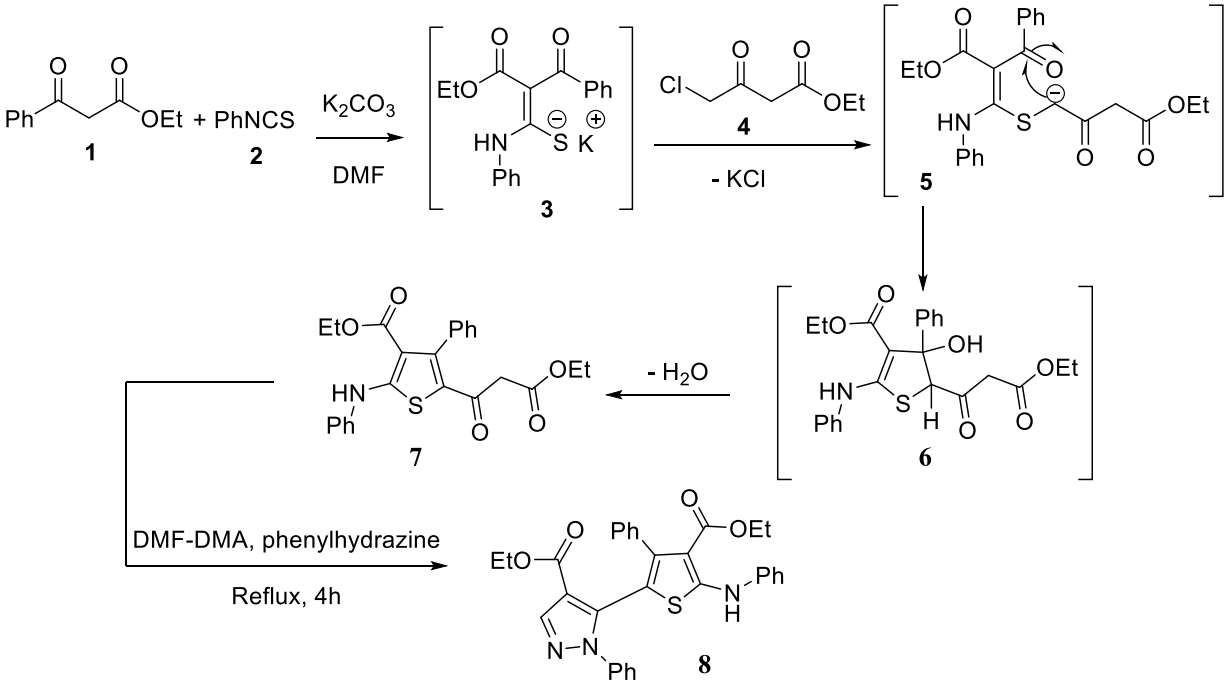

Scheme 1. Synthesis of thiophene **7** and thiophene pyrazole hybrid **8**.

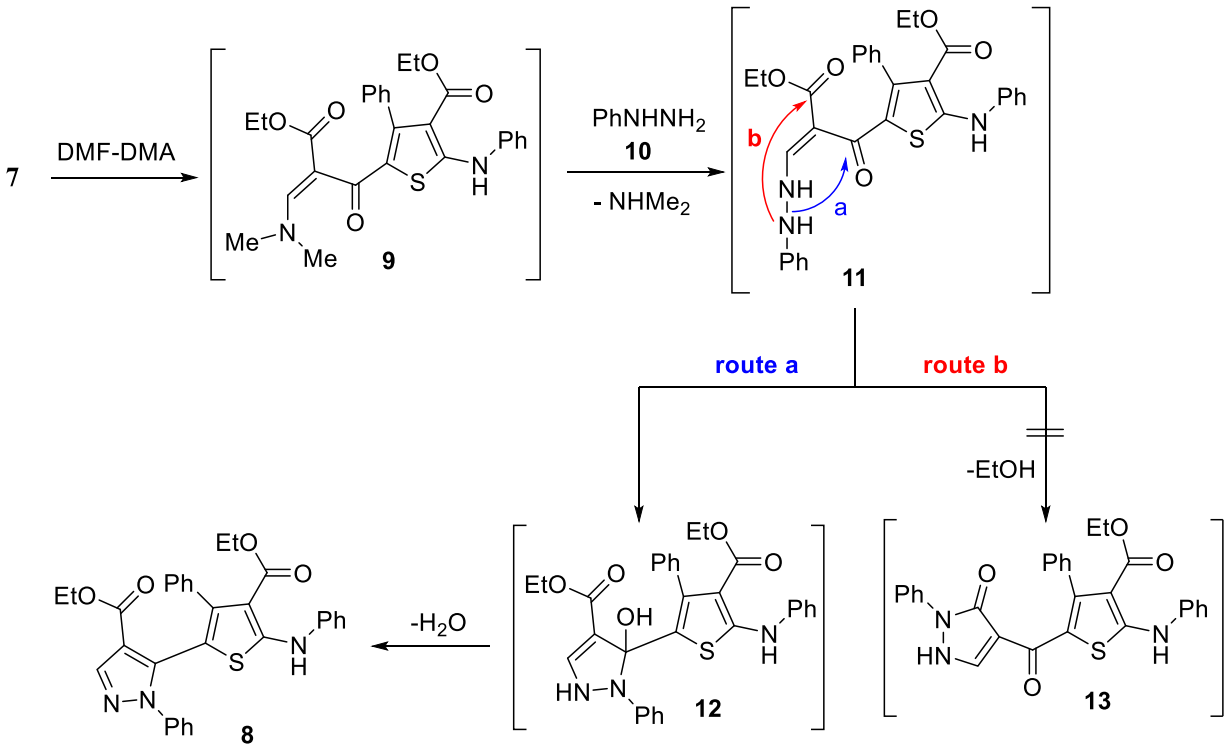

Scheme 2. Proposed mechanism for the synthesis of thiophene pyrazole hybrid **8**.

Table 1
X-ray data of compound **8**.

CCDC	2,519126
Empirical formula	$C_{31}H_{27}N_3O_4S$
Formula weight, g/mol	537.64
Temperature/K	293
Crystal system	Triclinic
Space group	P −1
a/Å	9.5962(7)
b/Å	11.6995(5)
c/Å	13.3105(10)
α/°	72.912(5)
β/°	87.789(6)
γ/°	87.619(5)
Volume/Å^3	1426.63(17)
Z	2
ρ_{calc} g/cm^3	1.252
μ/mm^{-1}	0.153
F(000)	564.5
Crystal size/mm^3	0.19 × 0.16 × 0.09
Crystal color, habit	Block, pale yellow
Radiation	Mo Kα (λ = 0.71073 Å)
2Θ range for data collection/°	3.19 to 26.91
Index ranges	−12 ≤ h ≤ 11, -13 ≤ k ≤ 15, -16 ≤ l ≤ 17
Reflections collected	18,939
Independent reflections	6066
Goodness-of-fit on F^2 (S)	1.018
R1, wR2 (I > 2σ (I))	R_1 = 0.0519, wR_2 = 0.1503
R1, wR2 [all data]	R_1 = 0.0831, wR_2 = 0.1503

Table 2
Selected X-ray vs DFT-optimized bond lengths (Å) and angles (°) for compound **8**.

Distances (Å)	X-ray	DFT	Distances (Å)	X-ray	DFT
S1–C2	1.7251(19)	1.7465	N2–C20	1.430(2)	1.429
S1–C3	1.7301(18)	1.7648	N3–C16	1.316(3)	1.322
N1-C2	1.362(2)	1.359	O2-C5	1.213(2)	1.231
N1-C8	1.401(3)	1.404	O1-C5	1.326(2)	1.343
N2-N3	1.3645(19)	1.3618	O4-C17	1.197(2)	1.214
N2-C14	1.365(2)	1.373	O3-C17	1.343(2)	1.355
Angles (°)	**X-ray**	**DFT**	**Angles (°)**	**X-ray**	**DFT**
C3-S1-C2	91.14(9)	91.53	O2-C5-O1	122.64(18)	121.48
C8-N1-C2	131.33(17)	131.63	O4-C17-O3	123.4(2)	123.20
C14-N2-N3	111.86(15)	112.40	C18-O3-C17	117.30(17)	115.76
C16-N3-N2	104.31(15)	105.21	C6-O1-C5	117.63(16)	116.46

fragment.

The results obtained by DFT optimization of compound **8** are in accordance with X-ray values as shown in Table 2, suggesting that the level of theory chosen in this study provides a reliable computational model for the interpretation of the reactivity and noncovalent interactions of the target molecule.

The molecule central conjugated segment is close to planar. The conjugation is extended from the thiophene ring toward the hydrazone-like linkage, which is supported by the torsion angle C14-N2-N3-C16 ≈ 179° (anti-arrangement), and C3-C14-N2-N3 ≈ 0° The ester substituents are also nearly coplanar with their attached carbonyls as C1-C5-O1-C6 and C15-C17-O3-C18 torsions are close to 0° This is consistent with the conjugative stabilization of the O—C = O fragment.

The structure of compound **8** in the crystal lattice is stabilized by intramolecular N—H•••O interaction between N1-H23 and the carbonyl oxygen O2 as shown in Fig. 4. This intramolecular hydrogen bond is stable and moderately bent and is consistent with the geometry (N1-H23 = 0.860 Å, H23•••O2 = 2.018 Å, N1•••O2 = 2.695 Å, and angle N—H•••O = 135.0° (Table 3). In addition, this interaction helps maintain planarity around the N1-C2 region due to the conformational lock supporting the electronic delocalization across the adjacent fragments.

No strong classical intermolecular hydrogen bonds were identified in the crystal lattice of compound **8**. Instead, the packing is stabilized primarily by van der Waals interactions with contributions from weak C6-H32b•••N3 and C28-H21•••O4 contacts, as shown in Table 4.

In addition, no significant π-π stacking is evident in compound **8**. The closest centroid-centroid separations are above the typical π-π stacking

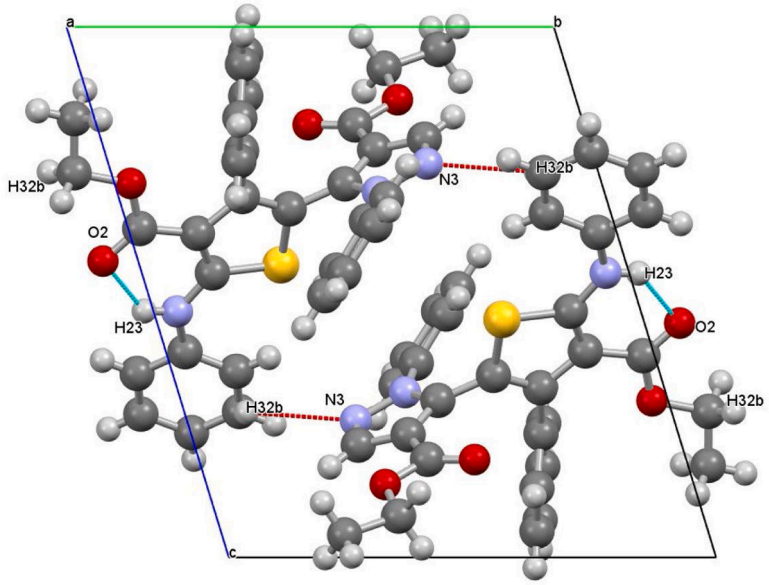

Fig. 4. Packing of compound **8** in the unit cell, viewed along the a-axis. Intramolecular interactions (turquoise) and intermolecular interactions (red) for compound **8** in the crystal.

Table 3
Intramolecular hydrogen bonds for compound **8** (Å and °).

D-H•••A	d(D-H)	d(H•••A)	d(D•••A)	<(DHA)	Symm. Code
N1-H23•••O2	0.860	2.018	2.695	135.0	x,y,z

Table 4
Selected weak intermolecular contacts for compound **8** (Å and °).

D-H•••A	d(D-H)	d(H•••A)	d(D•••A)	<(DHA)	Symm. Code
C6-H32B•••N3	0.970	2.662	3.254	119.7	x,y + 1,z
C28-H21•••O4	0.930	2.891	3.664	141.4	x + 1,y,z

interactions. This suggests that offset packing and dispersion-dominated contacts are more effective than π-π aromatic stacking.

Since suitable single crystals of compound **7** could not be obtained, the reliability of its optimized DFT geometry was evaluated by comparing the shared thiophene and carbonyl fragments with the experimental X-ray geometry of compound **8**, and with reported X-ray and DFT geometries of structurally related thiophene derivatives. The shared thiophene and carbonyl fragments for compounds **7** and **8** showed significant agreement as shown in Table 5. For example, the optimized S1-C2 and S1-C3 bond lengths and C3-S1-C2 angle in thiophene core of compound **7** show significant agreement with the experimental values of compound **8** and remain within the typical ranges reported for thiophenes. In addition, the calculated N1-C2, N1-C8, and the carbonyl C2=O5 and C1-O5 distances follow the same experimental trends, with small deviations expected because X-ray represents the solid-state structure, while DFT describes the gas phase. Similar small systematic differences between the X-ray geometries and B3LYP optimized structures have been reported for related thiophene derivatives, where the main ring and carbonyl metrics remain within the typical ranges and the small deviations are commonly due to the crystal packing forces and thermal motion [19,32,33]. For example, an X-ray and DFT study on diethyl 3-amino-5-((2-ethoxy-2-oxoethyl)thio)thiophene-2, 4-dicarboxylate optimized at B3LYP/6–311++G(d,p) showed consistency with calculated bond lengths and angles of compound **7**, with a small deviation attributed to solid state versus gas phase conditions such as S1-C1 (1.725 Å) and S1-C4 (1.730 Å) and C1-S1-C4 (92.51°) [19]. Another study on N-(thiophen2-ylmethyl)thiophene-2-carboxamide showed comparable agreement between its experimental XRD and DFT geometry of compound **7** with S1-C1 (1.694 Å), S1-C4 (1.707 Å), and C1-S1-C4 (92.2°) [32], supporting the suitability of this level of theory for describing thiophene bond metrics. Accordingly, the optimized geometry of compound **7** is considered reliable for the subsequent electronic property analyses such as MEP and FMO.

Table 5
Selected bond lengths (Å) and angles (°) for the shared thiophene and carbonyl fragments: experimental single crystal X-ray values for compound **8** and DFT optimized values for compound **8** and **7**.

Distances (Å)	X-ray (8)	DFT-optimized (8)	DFT-optimized (7)
S1–C2	1.7251(19)	1.7465	1.743
S1–C3	1.7301(18)	1.7648	1.770
N1-C2	1.362(2)	1.359	1.361
N1-C8	1.401(3)	1.404	1.411
O2-C5	1.213(2)	1.231	1.208
O1-C5	1.326(2)	1.343	1.377
Angles (°)	**X-ray (8)**	**DFT-optimized (8)**	**DFT-optimized (7)**
C3-S1-C2	91.14(9)	91.53	91.88
C8-N1-C2	131.33(17)	131.63	130.50
O2-C5-O1	122.64(18)	121.48	121.1
C2-N1-C8	131.3(2)	131.6	130.5

3.2.1. *Energy decomposition analysis of intermolecular interactions*

To quantify the driving forces for crystal packing of compound **8** beyond contact percentages, pairwise intermolecular interaction energies were evaluated using CE-B3LYP/6–31G(d,p) energy model implemented in the CrystalExplorer [25]. The total intermolecular energy (Etot) is obtained from scaled components comprising electrostatic (Eele), polarization (Epol), dispersion (Edis), and exchange-repulsion (Erep) factors as shown in Table 6. The calculated energies (Table 7) show that the dispersion is the dominant attractive contribution for the

Table 6
Scale factors for benchmarked energy models.

Energy Model	k_ele	k_pol	k_disp	k_rep
CE-B3LYP … B3LYP/6–31G(d,p) electron densities	1.057	0.740	0.871	0.618

Table 7
Interaction energy values of compound **8**.

	N	Symop	R	Electron Density	E_ele	E_pol	E_dis	E_rep	E_tot
	2	x, y, z	15.44	B3LYP/6-31G(d,p)	0.3	-0.0	-2.5	0.0	-1.9
	2	x, y, z	14.92	B3LYP/6-31G(d,p)	-2.2	-0.1	-5.8	0.0	-7.5
	1	-x, -y, -z	10.01	B3LYP/6-31G(d,p)	-2.7	-0.5	-20.6	7.0	-16.9
	1	-x, -y, -z	9.59	B3LYP/6-31G(d,p)	-11.7	-3.3	-70.1	34.9	-54.4
	2	x, y, z	9.60	B3LYP/6-31G(d,p)	-6.2	-2.2	-36.1	16.7	-29.2
	1	-x, -y, -z	11.18	B3LYP/6-31G(d,p)	-8.9	-2.2	-25.4	16.0	-23.3
	2	x, y, z	11.70	B3LYP/6-31G(d,p)	-5.3	-2.0	-14.9	11.2	-13.2
	1	-x, -y, -z	7.58	B3LYP/6-31G(d,p)	-9.6	-4.5	-93.4	44.6	-67.2
	1	-x, -y, -z	7.52	B3LYP/6-31G(d,p)	-8.1	-2.1	-65.4	29.0	-49.1
	1	-x, -y, -z	9.55	B3LYP/6-31G(d,p)	-6.3	-1.0	-49.4	25.8	-34.4
	1	-x, -y, -z	13.55	B3LYP/6-31G(d,p)	0.0	-0.0	-4.3	0.0	-3.7
	1	-x, -y, -z	14.04	B3LYP/6-31G(d,p)	-1.3	-0.3	-10.0	0.0	-10.4

most stabilizing molecular pairs. The summation of the attractive components over the listed molecular pairs indicates that dispersion accounts for approximately 83.2% of the stabilizing contribution, while the electrostatic and polarization contributions represent about 13.0% and 3.8%, respectively. This quantitative partitioning supports the Hirschfeld surface results, where H•••H and C•••H/ H•••C contacts are the most abundant. In addition, it indicates that the directional contacts involving heteroatoms contribute mainly through a smaller electrostatic component.

3.3. Hirshfeld surface analysis

The intermolecular interactions in the crystal packing of compound **8** were studied and visualized using Hirshfeld surface analysis and mapped over d_{norm}. The color scale indicates short and long contacts. Contacts shorter than the sum of van der Waals radii are represented by a red

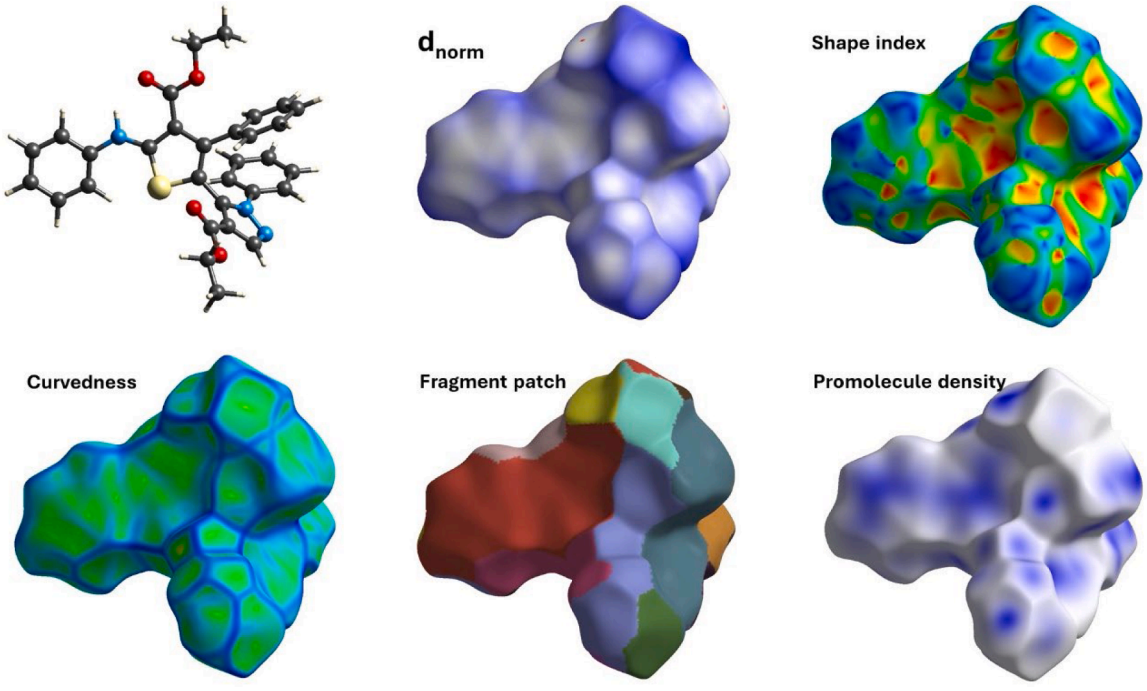

Fig. 5. Hirshfeld surface maps for compound **8** computed on the crystallographic geometry in CrystalExplorer. The surface is the standard Hirshfeld isosurface. The d_{norm} map scale ranges between −0.0144 and 2.0594. Shape index map scale ranges between −1.0000 and 1.0000.

color, contacts near van der Waals separation appear in white color, while longer contacts are shown in blue color. In compound **8**, the red color is focused near the oxygen atoms of the carbonyl group and the corresponding hydrogen atom on neighboring molecule (C28-H21•••O4), where oxygen atoms serve as the main acceptor sites for the short O•••H/H•••O in the crystal lattice as shown in Fig. 5. Another red spot is apparent around nitrogen atom as an acceptor and hydrogen atom on the adjacent molecule (C6-H32B•••N3). Although both interactions are weak, they help consolidate the crystal packing, especially in the absence of the classical intermolecular hydrogen bonding.

In addition, these observations are supported by fingerprint plots which provide a quantitative image of the intermolecular contacts, as shown in Fig. 6. The largest contribution in the crystal packing comes from H•••H contacts (57.9%), followed by C•••H/H•••C (18.6%) contacts. The O•••H/H•••O contacts contribute 10.6% consistent with the red spots concentrated around the carbonyl oxygen atoms. Smaller contributions arise from N•••H/H•••N (5.3%) and S•••H/H•••S (2.3%), indicating that nitrogen and sulfur participate as a secondary

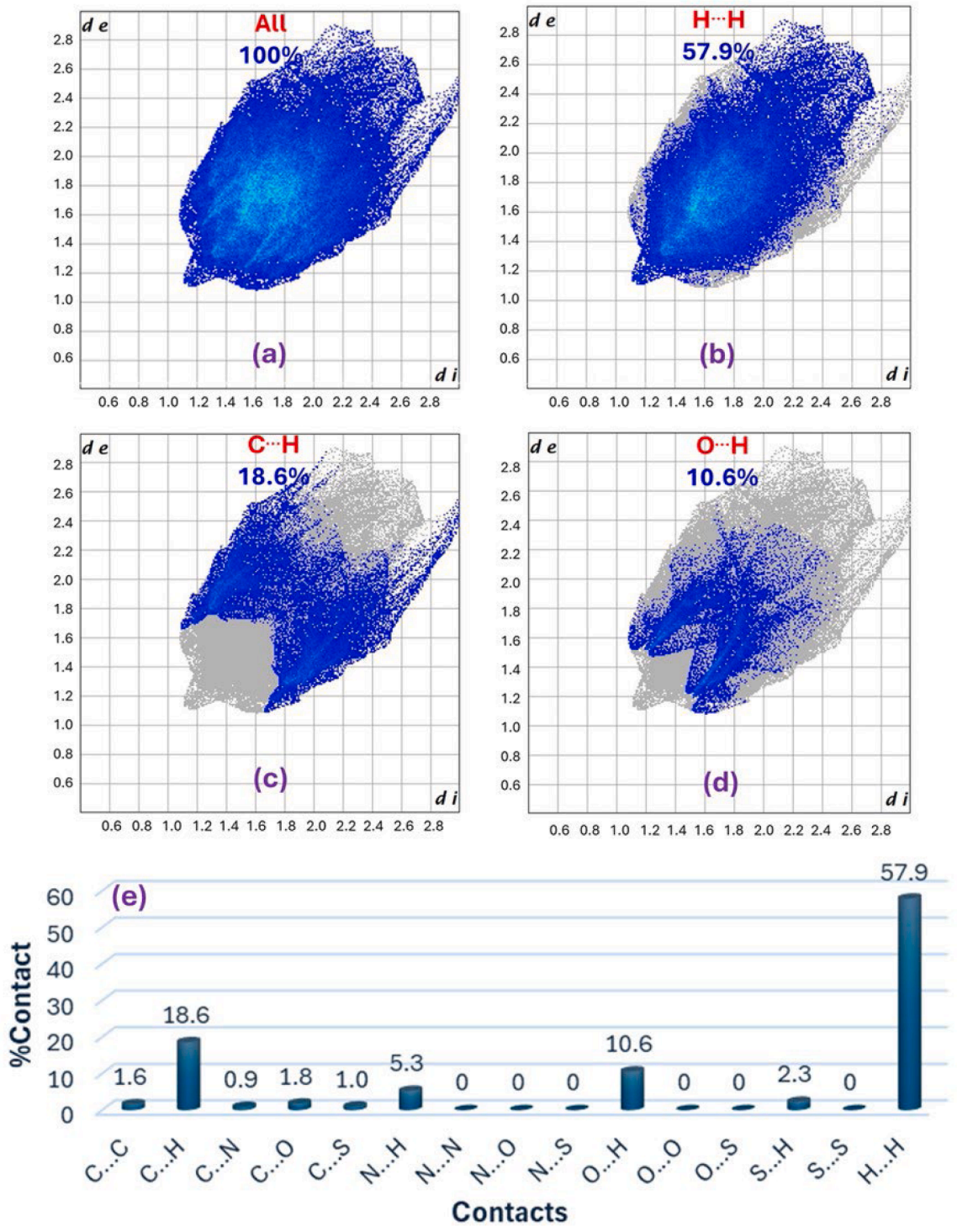

Fig. 6. Decomposed fingerprint plots (**a-d**) for the short contacts derived from the Hirshfeld surface of compound **8**, and non-covalent interactions (**e**) in compound **8**.

weak contact in the crystal packing. Other interactions including C•••O (1.8%), C•••C (1.6%), C•••S (1.0%), and C••N (0.9%) are minor, consistent with weak π–π stacking or heteroatom-heteroatom interactions.

The shape index and curvedness surfaces (Fig. 6) are consistent with this contact distribution. The small C•••C contribution indicates that any aromatic stacking is limited and localized rather than extended face to face packing.

3.4. Molecular electrostatic potential (MEP)

The molecular electrostatic potential (MEP) surface is a convenient way to visualize the charge distribution over the molecule therefore identifying the most probable regions for electrophilic and nucleophilic attack. The red regions correspond to negative potential sites while the blue regions represent the positive potential sites, and the green represents nearly neutral regions. The MEP map of compounds **7** and **8** (Fig. 7) shows the potential distribution over their surfaces within the range of −6.951e-2 to +6.951e-2 and −5.638e-2 to +5.638e-2, respectively. Compound **8** shows a slightly narrower range indicating that compound **7** exhibits a somewhat stronger overall electrostatic contrast across its surface compared with compound **8**.

In both compounds, the most negative potential is mainly concentrated around oxygen atoms of the carbonyl groups (O15, O16 and O17 in **7**, and O6 and O21 in **8**), and the nitrogen atom (N1) of the pyrazole ring in the optimized structure of **8**. This indicates strong electron richness regions marking them the preferred sites for electrophilic attack.

On the other hand, the light blue regions are concentrated around hydrogen atoms of the phenyl and ethyl groups in both compounds, reflecting relatively electron deficient hydrogen atoms. These atoms can act as weak donors in C—H based contacts. These results agree well with the intermolecular interactions inferred from the crystal lattice analysis in compound **8**.

3.5. Frontier molecular orbital (FMO) insights

Frontier Molecular Orbital (FMO) is a significant tool that helps rationalize the electronic properties and reactivity of the title compounds. The electron-donating tendency of the molecule is associated with the highest occupied molecular orbital (HOMO) while the electron accepting tendency is associated with the lowest unoccupied molecular orbital (LUMO). The ionization energy (IP) and the electron affinity (EA) of the title compound can be estimated from HOMO and LUMO energies where IP ≈ -E_{HOMO} and EA ≈ -E_{LUMO}. These values with the energy gap ($\Delta E = E_{LUMO} - E_{HOMO}$) are commonly used as an indicator of the compound's chemical hardness, stability, and reactivity.

Fig. 8 shows HOMO and LUMO plots for compounds **7** and **8**. Compound **7** exhibits HOMO = −5.611 eV and LUMO = −1.579 eV, with an energy gap of 4.032 eV, while compound **8** shows HOMO of −5.179 eV and LUMO of −1.054 eV, with a slightly larger energy gap of 4.125 eV. The small increase in compound **8** may be attributed to the introduction of the pyrazole ring and the additional aryl group which results in a modest stiffening of the electronic structure. This suggests that compound **8** is marginally less polarizable and slightly more resistant to charge transfer than compound **7**. However, the calculated Energy gap of both compounds falls in a moderate range indicating electronically stable molecules but still reactive under external perturbation, so they can participate in intermolecular recognition and donor-acceptor interactions.

As shown in Fig. 8, HOMO and LUMO densities in both compounds are mainly distributed over the conjugated π framework with a clear participation from the thiophene and adjacent aromatic ring. This indicates that these regions are the principal electron rich sites responsible for donor behavior. However, the LUMO densities are shifted toward the more electro-withdrawing portion of these molecules with increased contribution around the carbonyl containing fragments. This indicates that these regions are the principal centers for the acceptor capabilities of the title compounds. HOMO and LUMO densities distribution is consistent with intramolecular donor to acceptor character and agree with the MEP map, where oxygen atoms represent the most negative potential sites.

The global reactivity descriptors of compounds **7** and **8** were derived from the HOMO and LUMO energies (Table 8) based on the following formulas [34]:

$$\text{Hardness}: \ \eta = \frac{IP - Ea}{2}$$

$$\text{Chemical potential}: \ \mu = -\frac{(IP + Ea)}{2}$$

$$\text{Softness}: \ S = \frac{1}{\eta}$$

$$\text{Electronegativity}: \ \chi = \frac{IP + Ea}{2}$$

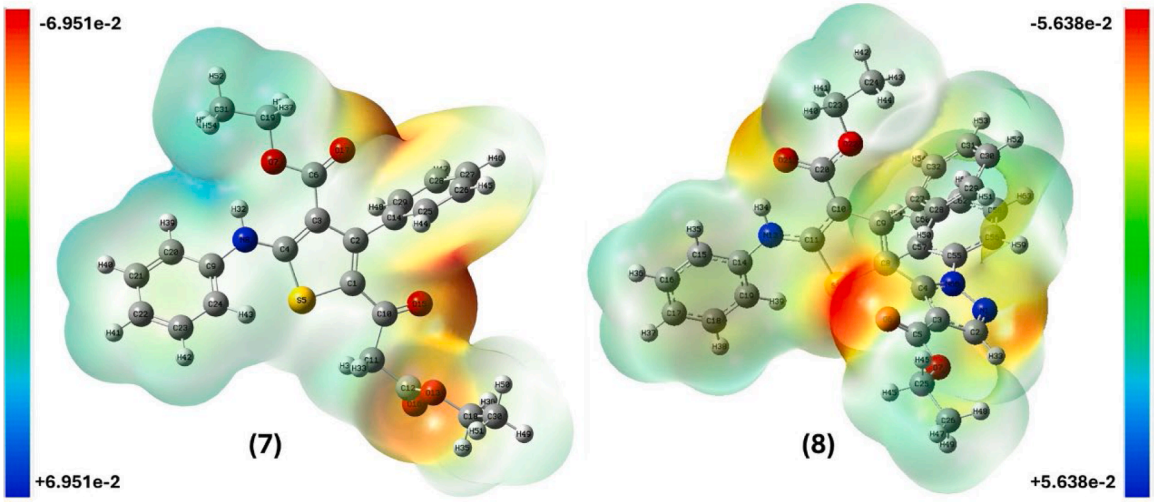

Fig. 7. The MEP map for optimized compounds **7** and **8** using density functional theory (DFT) with the B3LYP method and basis sets of 6–311++G(d,p) under neutral conditions.

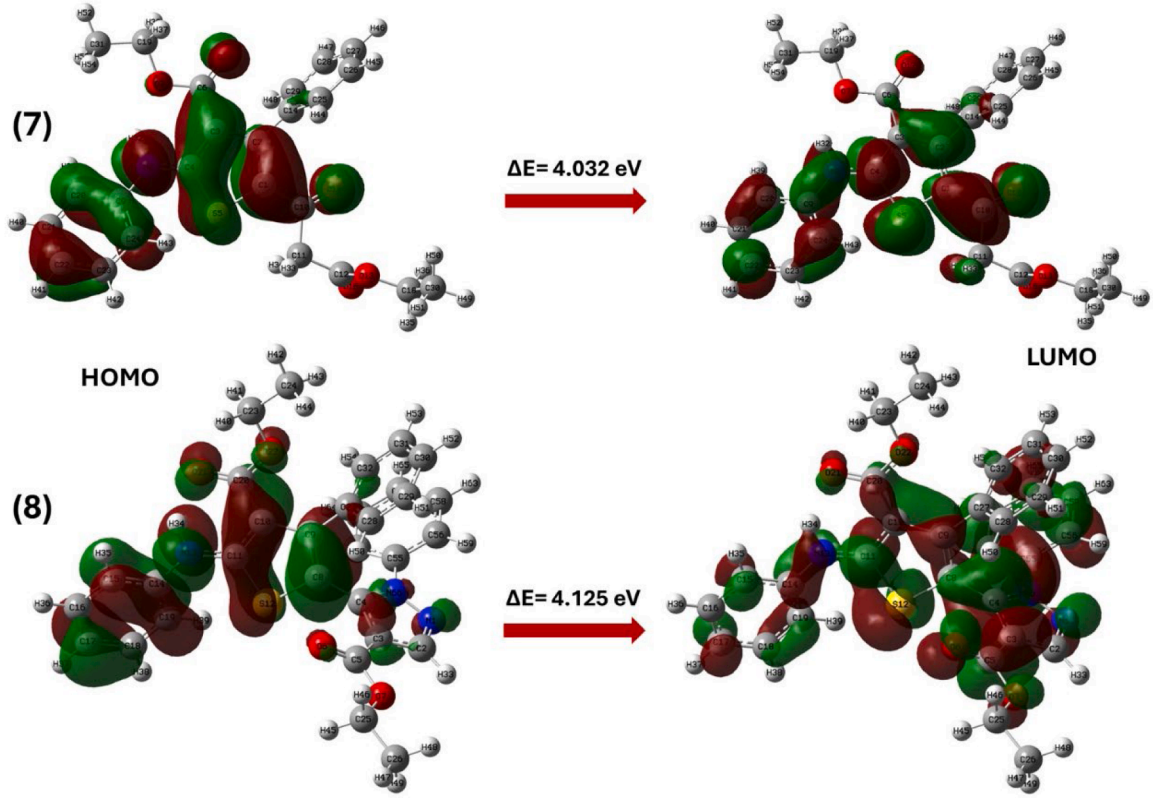

Fig. 8. The HOMO and LUMO levels for the optimized compounds **7** and **8**, calculated using DFT at the B3LYP/6–311++G(d.p).

Table 8
HOMO, LUMO, ionization potential (IP), electron affinity (Ea), chemical potential (μ), chemical hardness (η), softness (S), and electronegativity (χ) of compounds **7** and **8** in eV calculated using HOMO/LUMO energies.

Reactivity parameters	7	8
HOMO (eV)	−5.611	−5.179
LUMO (eV)	−1.579	−1.054
Ionization potential (IP)	5.611	5.179
Electron affinity (Ea)	1.579	1.054
Chemical potential (μ)	−3.595	−3.117
Chemical hardness (η)	2.016	2.062
Softness (S)	0.496	0.485
Electronegativity (χ)	3.595	3.117

Ionization potential of compounds **7** and **8** was found to be 5.611 and 5.179 eV, while electron affinity was found 1.579 and 1.054, respectively. Compound **7** shows a slightly higher ionization potential and electron affinity than **8**, which is consistent with the difference in orbital stabilization upon structural modification. In addition, compound **8** showed a slightly higher hardness (2.062 eV) than **7** (2.016 eV) in agreement with its larger HOMO-LUMO gap value, indicating a reasonable resistance to charge transfer. The softness follows the same trend (0.496 eV^{-1} for **7** and 0.485 eV^{-1} for **8**) indicating that both molecules retain appreciable electronic flexibility, which can facilitate weak donor-acceptor interactions and polarization in condensed phases, and slightly higher for compound **7**. In addition, the negative chemical potential for compounds **7** and **8** (−3.595 and −3.117 eV, respectively) and the electronegativity value (3.595 and 3.117 eV, respectively) reflect a stronger tendency for compound **7** to attract electron density, which may be attributed to the distribution of the electron acceptor centers such as the carbonyl groups and heteroatoms and the overall polarization in this compound.

3.6. NBO charge and Mulliken population analysis

The electron density distribution across the optimized compound is further studied using Natural Bond Orbital (NBO) and Mulliken population analysis. NBO and Mulliken descriptors provide complementary views of the molecular polarization; however, NBO is less sensitive to the choice of basis set artifacts.

In compounds **7** and **8**, the most electron-rich centers are associated with the heteroatoms and selected atoms within the conjugated framework, as shown in Fig. 9 and Tables 9 and 10. The large negative charges are observed at the oxygen atoms and the more electronegative nitrogen sites, consistent with their role as preferred regions of electron density. In compound **7** (Table 9 and Fig. 9), the negative charge in Mulliken and NBO is mainly focused on the carbonyl and ester oxygens such as O13, O15, O16, and O16, while the amine nitrogen N8 shows a pronounced negative charge. These results indicate that oxygen atoms are the dominant electron density reservoirs and the most preferred favorable acceptor sites for electrophilic attack, and for noncovalent recognition, in agreement with The MEP surface findings. In consistent with the conjugation, several carbon atoms within the aromatic or delocalized framework also carry partial negative charge. In addition, C30 and C31 of the ethyl groups show high negative charges (Mulliken −0.48492 and −0.49641, NBO −0.70219 and −0.70635, respectively). In compound **8** (Table 10 and Fig. 9), the results show a closely related pattern to compound **7** where the negative charge is observed at O1 and O22 (Mulliken −0.476 and −0.353, NBO −0.648 and −0.532), the carbonyl/ester oxygen atoms O6 and O7 (Mulliken −0.422 and −0.368, NBO −0.589 and −0.550), and N13 which carries the most negative (Mulliken −0.704, NBO −0.577) confirming these sites as strong electron donor centers within the molecular scaffold. In addition, several carbon atoms in aromatic and conjugated fragments exhibit negative charge, such as C15, C16, C19, and C28-C32, where these atoms are part of a delocalized π system, and the electron density is not confined to heteroatoms alone.

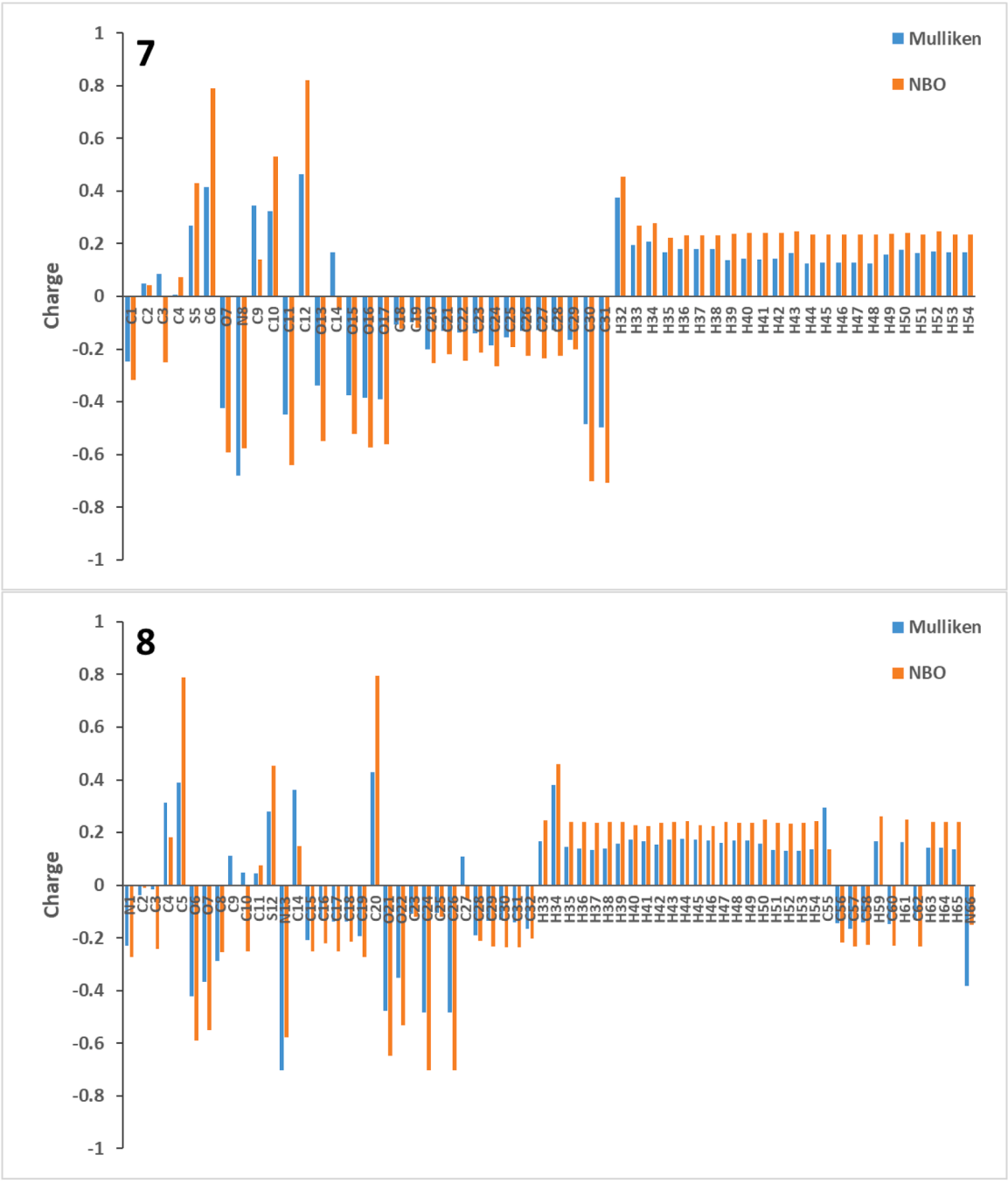

Fig. 9. Plots of NBO and Mulliken charge for the optimized compounds **7** and **8**, calculated using DFT with the B3LYP method and basis sets of 6–311++G(d,p) under neutral conditions.

In contrast, several atoms exhibit strong positive polarization, particularly carbon atoms that are directly attached to electronegative atoms. In compound **7**, carbon atoms of the carbonyl groups show high positive polarization such as C6 (Mulliken 0.416368 and NBO 0.78896) and C12 (Mulliken 0.462606 and NBO 0.8203)consistent with carbonyl activation. Several additional atoms display moderate positive charges such as C9 and C10 indicating localized polarization near the substituted or heteroatom adjacent positions. Compound **8** shows similar trend. The carbonyl carbons (C5 and C20) showed the strongest positive character (Mulliken 0.388 and 0.430, NBO 0.789 and 0.795), indicating high electron-deficient centers. Several additional carbon atoms show moderate positive charges, such as C4, C14, and C55, indicating their susceptibility to nucleophilic attack. In both compounds, sulfur atoms S5 in & and S12 in 8 showed interesting behavior with a positive charge in both analyses (S5: Mulliken 0.270019, NBO 0.4308 and S12: Mulliken 0.280, NBO 0.455). This uncommon behavior may be attributed to the electronic environment where sulfur does not act as an electron-rich site; instead, overall polarization is driven strongly by the oxygen and nitrogen atoms and the conjugated framework. These results are consistent with our reported work [35]. All hydrogen atoms in both compounds, as expected, exhibit a positive charge, and the magnitude varies with their local bonding environment. H32 is the most positive hydrogen in compound **7**, while the most aromatic and aliphatic hydrogens fall within smaller positive charges. In compound **8**, H34 (attached to N13) exhibits the highest positive charge among hydrogen atoms (Mulliken 0.381, NBO 0.460), while most aromatic and aliphatic

Table 9
NBO and Mulliken charge for compound **7**.

Atom	Charge		Atom	Charge	
	Mulliken	NBO		Mulliken	NBO
C1	−0.24606	−0.31866	C28	−0.129357	−0.22645
C2	0.048585	0.04389	C29	−0.165811	−0.20142
C3	0.086191	−0.25153	C30	−0.48492	−0.70219
C4	0.006925	0.07344	C31	−0.49641	−0.70635
S5	0.270019	0.4308	H32	0.374047	0.45407
C6	0.416368	0.78896	H33	0.196602	0.2679
O7	−0.424435	−0.5913	H34	0.206193	0.27619
N8	−0.679504	−0.57786	H35	0.167189	0.22282
C9	0.344644	0.14022	H36	0.180303	0.23106
C10	0.322451	0.53148	H37	0.179064	0.23133
C11	−0.448242	−0.63949	H38	0.180185	0.23214
C12	0.462606	0.8203	H39	0.137939	0.23668
O13	−0.340065	−0.54805	H40	0.142618	0.24177
C14	0.167047	−0.0502	H41	0.139774	0.24099
O15	−0.376277	−0.52196	H42	0.144502	0.24241
O16	−0.384859	−0.57448	H43	0.164561	0.24766
O17	−0.390918	−0.5615	H44	0.126051	0.23555
C18	−0.107756	−0.12138	H45	0.128285	0.23437
C19	−0.097144	−0.11759	H46	0.127281	0.23357
C20	−0.202807	−0.25198	H47	0.128811	0.23458
C21	−0.130723	−0.21853	H48	0.125567	0.23467
C22	−0.136743	−0.24527	H49	0.15914	0.23879
C23	−0.139229	−0.21499	H50	0.17565	0.24108
C24	−0.185468	−0.26521	H51	0.164797	0.23494
C25	−0.154593	−0.19348	H52	0.171646	0.2472
C26	−0.130332	−0.22616	H53	0.167231	0.23485
C27	−0.129652	−0.23343	H54	0.169035	0.23574

Table 10
NBO and Mulliken charge for compound **8**.

Atom	Charge		Atom	Charge	
	Mulliken	NBO		Mulliken	NBO
N1	−0.228808	−0.27276	H34	0.381422	0.45996
C2	−0.03641	−0.00936	H35	0.144915	0.23977
C3	−0.014874	−0.24128	H36	0.138259	0.23964
C4	0.312276	0.18165	H37	0.133417	0.23797
C5	0.388073	0.78933	H38	0.138536	0.23935
O6	−0.421759	−0.58879	H39	0.157866	0.24135
O7	−0.36755	−0.55006	H40	0.171532	0.22668
C8	−0.288403	−0.25559	H41	0.16773	0.22383
C9	0.111119	−0.0027	H42	0.155848	0.23696
C10	0.04717	−0.25265	H43	0.173315	0.24053
C11	0.046134	0.07428	H44	0.17584	0.24168
S12	0.279568	0.45451	H45	0.172572	0.22679
N13	−0.704247	−0.57718	H46	0.16914	0.22461
C14	0.361671	0.14824	H47	0.160634	0.23965
C15	−0.207098	−0.25188	H48	0.168638	0.23712
C16	−0.130434	−0.2196	H49	0.170172	0.23803
C17	−0.139509	−0.25224	H50	0.157151	0.25034
C18	−0.139392	−0.21564	H51	0.132483	0.23638
C19	−0.194388	−0.27174	H52	0.129877	0.23478
C20	0.42978	0.79531	H53	0.130261	0.23561
O21	−0.476263	−0.64832	H54	0.136644	0.24202
O22	−0.353179	−0.53208	C55	0.29465	0.13599
C23	−0.107511	−0.1191	C56	−0.14588	−0.21756
C24	−0.483285	−0.70208	C57	−0.167225	−0.23322
C25	−0.103456	−0.1202	C58	−0.140977	−0.22731
C26	−0.483629	−0.70198	H59	0.165611	0.26043
C27	0.110034	−0.05382	C60	−0.147174	−0.22844
C28	−0.18959	−0.21059	H61	0.163528	0.24873
C29	−0.136574	−0.23319	C62	−0.130796	−0.23448
C30	−0.133487	−0.23517	H63	0.140803	0.24086
C31	−0.140527	−0.23744	H64	0.141685	0.24142
C32	−0.166369	−0.20147	H65	0.13712	0.239
H33	0.166734	0.24652	N66	−0.383414	−0.15136

hydrogens fall in the typical positive charge range, indicating their potential role as donors in weak intermolecular contacts.

Overall, the results indicate an agreement in trends between NBO and Mulliken charge analyses, despite the differences in the absolute values. In addition, NBO and Mulliken charge analyses reveal a polarization within compounds **7** and **8** consistent with the reactivity and noncovalent interaction tendencies inferred from MEP and FMO results.

3.7. Physicochemical and pharmacokinetic parameters

To assess the oral drug-likeness profile of compounds **7** and **8**, a comprehensive *in silico* physicochemical analysis was conducted. The calculated values are presented in Table 11.

As shown in Table 11 and Fig. 10, thiophene **7** exhibits moderate aqueous solubility and good gastrointestinal (GIT) absorption, as indicated by its position within the white region of the BOILED-Egg diagram. Additionally, it complied with several desirable drug-likeness criteria, including Lipinski's and Egan's rules.

In contrast, thiophene pyrazole hybrid **8** showed poor aqueous solubility, alongside poor gastrointestinal absorption and blood–brain barrier permeability (BBB). Nevertheless, it exhibited a moderate synthetic accessibility score and, similar to **7**, did not display any PAINS alerts, indicating a low likelihood of toxic traits commonly associated with problematic scaffolds [36]. Overall, both compounds demonstrated moderate synthetic accessibility and were free from PAINS alerts, supporting their potential suitability as drug-like molecules.

3.8. Docking performance

Thiophene and pyrazole moieties have been widely investigated in literature for their promising anticancer potential, particularly against solid tumors such as breast, colon, and liver cancers. Among the molecular targets implicated in these malignancies, the epidermal growth factor receptor (EGFR) represents an attractive therapeutic target, as it plays a central role in regulating cellular proliferation, survival, and differentiation, and its overexpression is particularly dominant in solid tumours [37].

Molecular docking studies demonstrated that thiophene **7** exhibited a binding mode notably similar to that of the standard drug Erlotinib and the co-crystallized ligand 8 BM within the EGFR active site (Table 12 and Fig. 11). It formed a total of two hydrogen bonds, a key hydrogen bond with ATP-Pocket residue Cys797, similar to both reference ligands, in addition to an extra hydrogen bond with Thr854, suggesting a more stable and extensive binding pattern. In contrast, thiophene pyrazole hybrid **8**, displayed a less favorable interaction profile, despite showing a comparable binding energy. It formed a single hydrogen bond with Ser720 and interacted with Cys797 via a π–sulfur interaction rather than a conventional hydrogen bond. Moreover, its interaction with Thr854 was predominantly hydrophobic, accompanied by several additional hydrophobic contacts within the binding pocket. Both compounds demonstrated extensive hydrophobic interactions with several critical amino acid residues in the EGFR active site, including Leu718, Val726, Met793, and Leu844 [38].

These findings suggest that compound **7** may exhibit greater binding stability within the EGFR catalytic pocket than compound **8**, potentially supporting its further investigation as a promising EGFR inhibitor candidate.

The docking results of the thiophene pyrazole hybrid **8** are in agreement with the reported anticancer activities of the analogous examples **I-VI** (Fig. 12) [39–41]. These results indicat that the hybridization of the thiophene ring with the pyrazole moiety improves the binding interactions with the anticancer targets in the cancer cell.

3.9. In silico toxicity risk and drug likeness evaluation

A preliminary *in silico* evaluation of compounds **7** and **8** was conducted using the OSIRIS Property Explorer interface, which provides a fast color-coded screening of a compound's pharmaceutical viability [31]. Toxicity risk analysis showed that both compounds have low risk

Table 11
ADME Pharmacokinetics and Drug likeness parameter of compounds **7** and **8**.

Compound 7				Compound 8			
Physicochemical		Lipophilicity		Physicochemical		Lipophilicity	
Formula	$C_{24}H_{25}NO_5S$	Log Po/w (iLOGP)	3.80	Formula	$C_{31}H_{27}N_3O_4S$	Log Po/w (iLOGP)	4.79
Molecular weight	439.52	Log Po/w (XLOGP3)	5.12	Molecular weight	537.63	Log Po/w (XLOGP3)	7.76
Num of heavy atoms	31	Log Po/w (WLOGP)	4.09	Num. of heavy atoms	39	Log Po/w (WLOGP)	7.36
Num. of arom. Heavy atoms	12	Log Po/w (MLOGP)	2.55	Num. of arom. Heavy atoms	28	Log Po/w (MLOGP)	4.6
Fraction Csp3	0.29	Log Po/w (SILICOS-IT)	4.28	Fraction Csp3	0.13	Log Po/w (SILICOS-IT)	6.7
Num. rotatable bonds	11	Consensus Log Po/w	3.97	Num. rotatable bonds	11	Consensus Log Po/w	6.24
Num. H-bond acceptor	5	**Water Solubility**		Num. H-bond acceptor	5	**Water Solubility**	
Num. H-bond donor	1	Log S (ESOL)	−5.35	Num. H-bond donor	1	Log S (ESOL)	−7.87
Molar Refractivity	121.68	Solubility(mg \ml)	1.96e-03 mg/ml	Molar Refractivity	154.03	Solubility(mg \ml)	0.0000073
TPSA	107	Class	Moderately soluble	TPSA	110.69	Class	Poorly soluble
Pharmacokinetics		Log S (Ali)	−7.11	**Pharmacokinetics**		Log S (Ali)	−9.93
GI absorption	High	Ali Solubility (mg \ml)	3.40e-05 mg/ml	GI absorption	Low	Ali Solubility (mg \ml)	0.0000000634
BBB permeation	No	Class	Poorly soluble	BBB permeation	No	Class	Poorly soluble
P-gp substrate	No	Log S (SILICOS-IT)	−6.90	P-gp substrate	No	Log S (SILICOS-IT)	−10.54
CYP1A2 inhibitor	Yes	Solubility (mg \ml)	5.58e-05 mg/ml	CYP1A2 inhibitor	No	Solubility (mg \ml)	0.0000000155
CYP2C19 inhibitor	Yes	Class	Poorly soluble	CYP2C19 inhibitor	Yes	Class	Insoluble
CYP2C9 inhibitor	Yes	**Drug likeness**		CYP2C9 inhibitor	Yes	**Drug likeness**	
CYP2D6 inhibitor	Yes	Lipinski	Yes, 0 violations.	CYP2D6 inhibitor	No	Lipinski	No; 2 violations W > 500, MLOGP>4.15
CYP3A4 inhibitor	Yes	Ghose	Yes	CYP3A4 inhibitor	Yes	Ghose	No; 3 violations MW>480, WLOGP>5.6, MR>130
Log k_p (Skin permeation)	−5.35	Veber	No 1 violation: Rotors>10	Log k_p (Skin permeation)	−4.07	Veber	No 1 violation: Rotors>10
Medicinal Chemistry		Egan	Yes	**Medicinal Chemistry**		Egan	No, 1 violation: WLOGP>5.88
PAINS	0 alert	Muegge	No; 1 violation: XLOGP3>5	PAINS	0 alert	Muegge	No; 1 violation: XLOGP3>5
Brenk	2 alert: >2 esters, beta keto anhydride	Bioavailability Score	0.55	Brenk	1 alert: >2 esters	Bioavailability Score	0.17
Synthetic accessibility	4.92			Synthetic accessibility	4.54		

(green), with no structural alerts regarding the four major risk classes: mutagenicity, tumorigenicity, irritancy, or reproductive toxicity (Table 13). This preliminary safety profile is encouraging, as the absence of structural alerts in these categories is often associated with low risk during preclinical safety testing.

In physicochemical profile and drug-likeness assessment, the calculated molecular weight of compound **7** is 437.0 g mol^{-1} which remains below the 500 g mol^{-1} guideline often used for oral drug candidates (Lipinski's rule of five) [36,42], while compound **8** (537.0 g mol^{-1}) exceeds the guideline threshold (Table 13). The predicted lipophilicity (cLogP 5.11 for **7** and 6.62 for **8**) is higher than the Lipinski threshold of 5 for both compounds, suggesting a hydrophobic character that may affect their aqueous solubility. The estimated aqueous solubility for both compounds is low (LogS = −6.74 for **7** and −7.75 for **8**), which is consistent with the predicted lipophilicity, with compound 8 being less soluble than compound **7**, in agreement with its higher cLogP and larger molecular size. Nevertheless, the topological polar surface area (TPSA) values (109.9 and 110.6 $Å^2$ for **7** and **8**, respectively) remain within the common range of appropriate permeability (<140 Å). In addition, there is a big difference between compound **7** (−20.9) and **8** (0.96) in the fragment-based drug-likeness values, suggesting the presence of fragments in **8** frequently found in bioactive molecules. The overall drug-score is low for both compounds (0.18 for **7** and 0.19 for **8**) due to the high lipophilicity and low predicted solubility. The multiple heteroatoms in these molecules increase the polarity and maintain TPSA near 110 $Å^2$, which is compatible with the membrane permeability. However, the aromatic system and the bulky hydrophobic framework increase the cLogP and reduce the predicted solubility.

These findings showed that compounds **7** and **8** indicate no predicted toxicity alerts in the four major risks. In addition, TPSA remains within the range commonly associated with membrane permeability, with a positive drug-likeness. However, the high lipophilicity and low predicted solubility suggest a future optimization to improve the solubility and reduce the lipophilicity.

4. Conclusion

Efficient one-pot synthetic methods for thiophene **7** and a thiophene-pyrazole hybrid **8** were reported. Their chemical structures were confirmed using IR, NMR, and MS spectroscopic techniques.

Single-crystal X-ray diffraction confirmed the molecular structure of compound **8** and provided crystal packing for this compound.

The crystallographic analysis shows that the crystal lattice of compound **8** is stabilized mainly by weak C—H•••O and C—H•••N

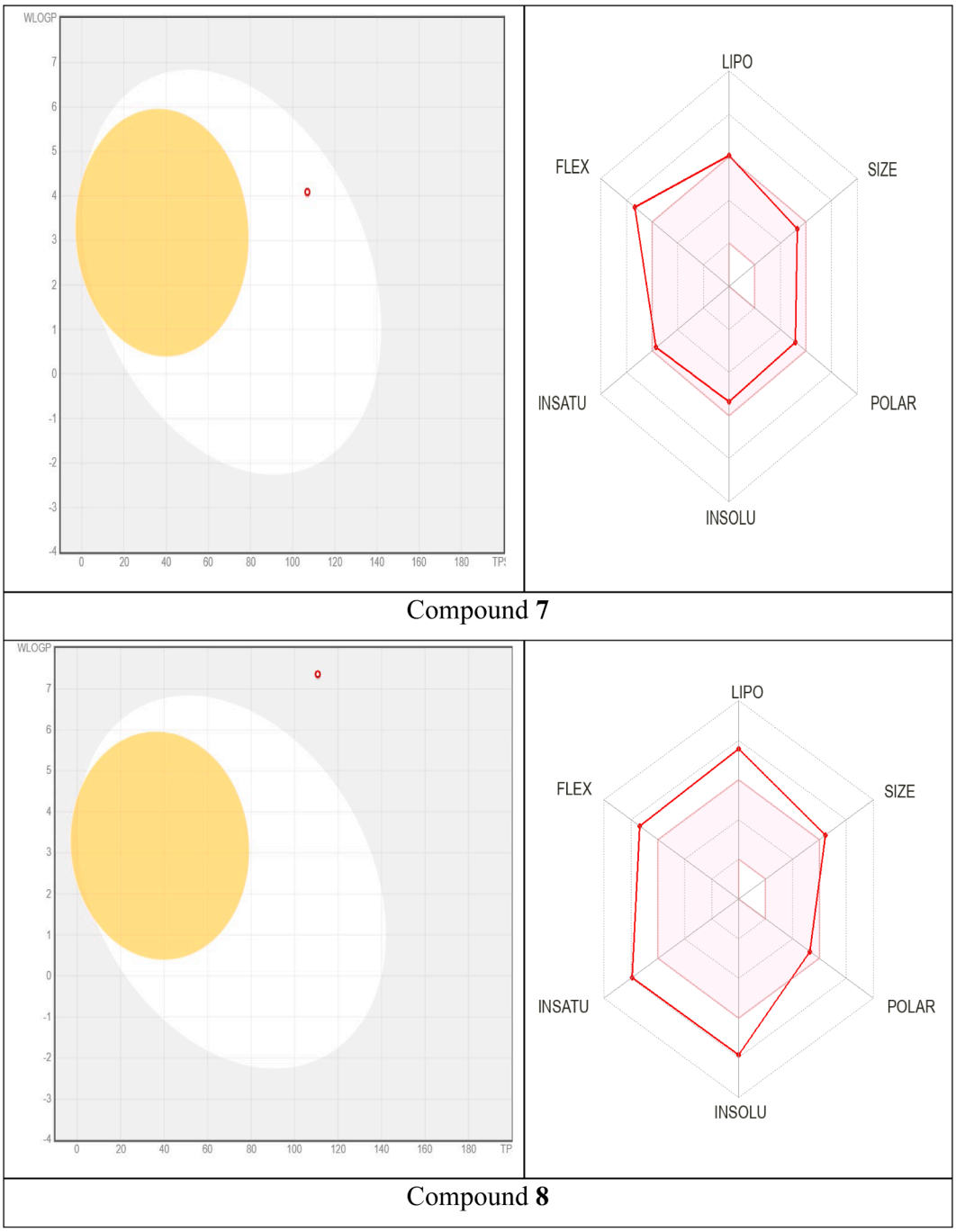

Fig. 10. *In silico* ADME prediction of compounds **7** and **8** using the BOILED-Egg model and bioavailability radar.

Table 12
Binding affinity (Kcal mol^{-1}) and type of interactions of the compounds **7, 8**, Erlotinib, and 8 BM inside the EGFR kinase (5UGB).

Origin	Molecule	Activation Energy (Kcal mol^{-1})	Interacting Atom	Type of interaction	Bond Length (A°)	Amino Acid
EGFR kinase (PDB ID: 5UGB)	Compound **7**	−6.9	=O	H bond acceptor	2.23	CYS 797
					2.91	THR 854
	Compound **8**	−6.8	=O	H bond acceptor	3.20	SER 720
	Erlotinib	−6.6	- O -	H bond acceptor	2.36	CYS 797
					2.45	
	8BM	−8.4	Cyclic nitrogen	H bond acceptor	3.21,3.30	MET 793
			-N-	H bond donor	3.00	CYS 797
			=O			

The docking protocol was validated by redocking the co-crystallized ligand, achieving an RMSD of <2 Å.

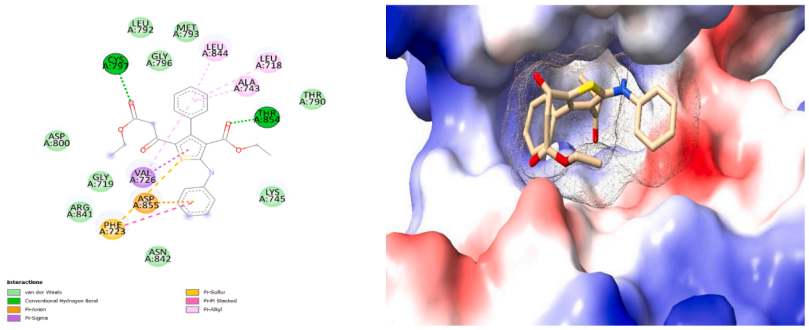

(A) Compound **7**

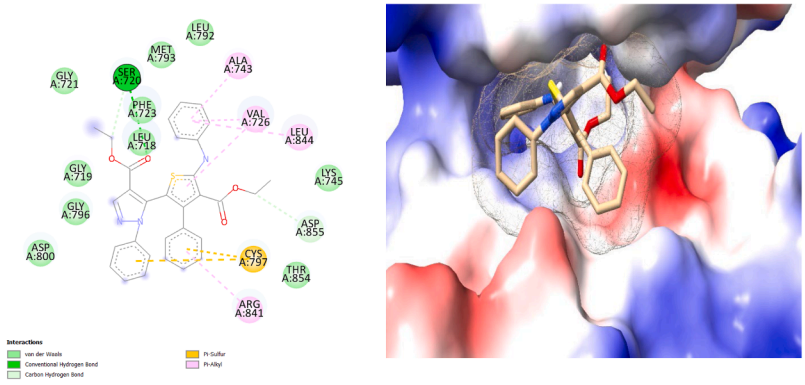

(B) Compound **8**

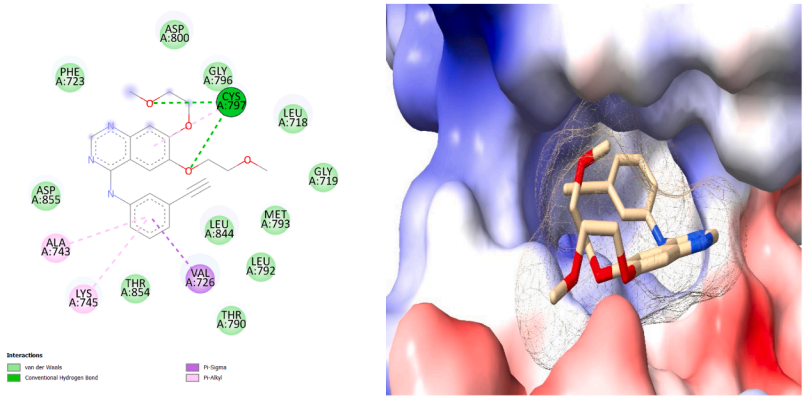

(C) Erlotinib

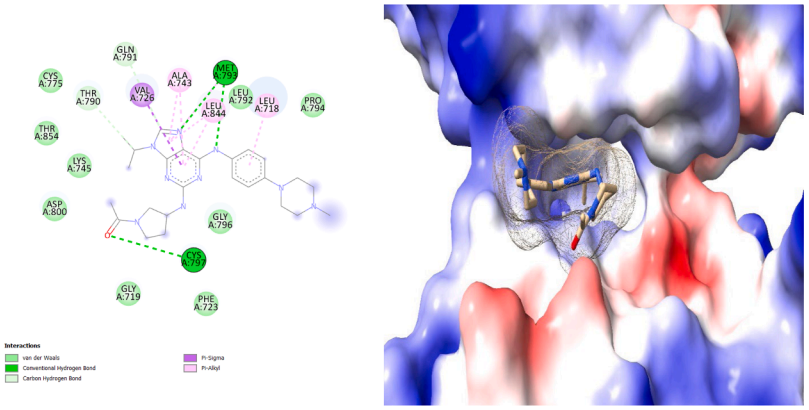

(D) 8BM

Fig. 11. 2D, 3D Visualization of compounds **7, 8**, Erlotinib, and 4-hydroxytamoxifen docked in the pocket of the 5UGB protein.

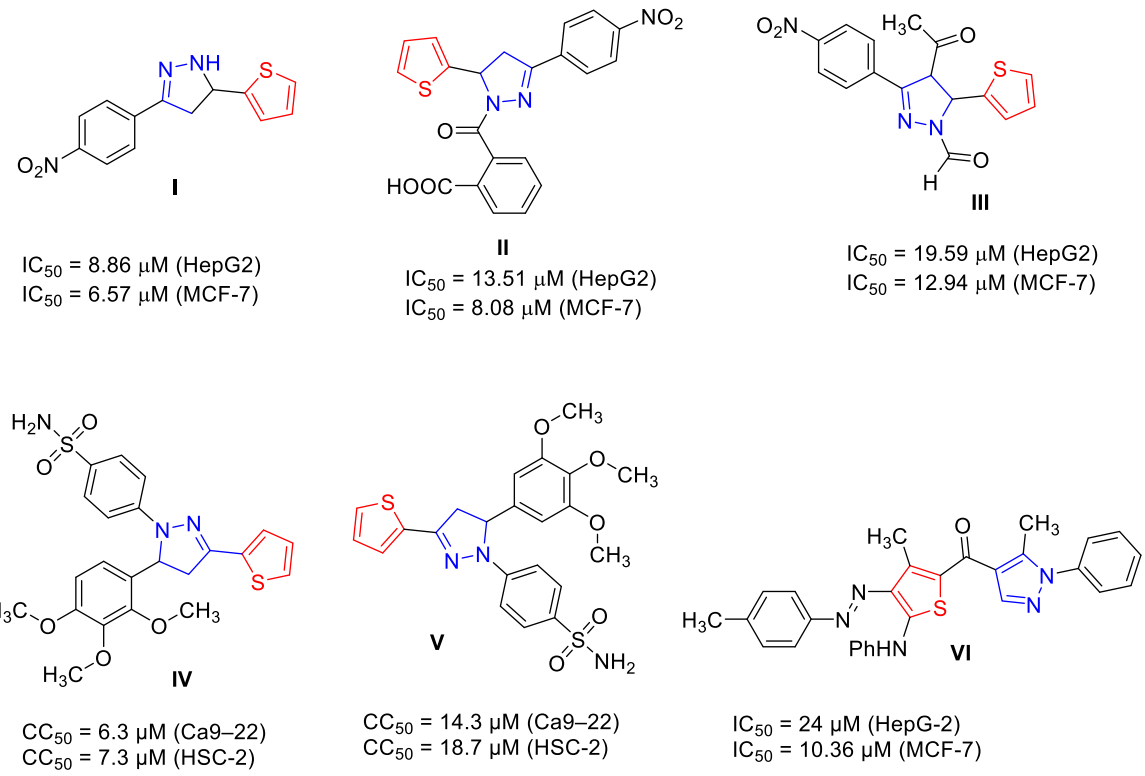

Fig. 12. Reported anticancer activities of thiophene pyrazole hybrids **I-VII**.

Table 13
The predicted physicochemical properties and toxicity risks of compounds **7** and **8** were generated by the OSIRIS Property Explorer interface.

Analysis	Compound 7	Compound 8
Mutagenicity		
Tumorigenicity		
Irritancy		
Reproductive effectiveness		
Molecular weight (MW, g mol^{-1})	437.0	537.0
Partition coefficient (cLogP)	5.11	6.62
Aqueous solubility (mol L^{-1})	−6.74	−7.75
Topological polar surface area (TPSA, $Å^2$)	109.9	110.6
Drug likeness	−20.9	0.96
Drug-Score (0–1)	0.18	0.19

interactions and supported by dominant H•••H and C•••H dispersive contacts, in agreement with the Hirshfeld surface analysis.

DFT calculations for both compounds indicate moderate HOMO/LUMO gap (4.032 for **7** and 4.125 eV for **8**), the hardness (2.016 for **7** and 2.062 eV for **8**), and softness (0.496 eV^{-1} for **7** and 0.485 eV^{-1} for **8**) of these compounds indicate a reasonable resistance to charge transfer, which is consistent, and the molecules retain some electronic flexibility, which can facilitate weak donor-acceptor interactions and polarization in condensed phases, although compound **8** is marginally less polarizable and slightly more resistant to charge transfer than compound **7**. The MEP analysis, NBO, and Mulliken charge analyses identify oxygen and nitrogen atoms as the principal electron-rich sites. In addition, ORASIS evaluation indicated no major toxicity alerts for mutagenicity, tumorigenicity, irritancy, and reproductive risks for compounds **7** and **8**, although the predicted high lipophilicity and low solubility affected the overall drug score. Complementary *in silico* ADME prediction and molecular docking studies were conducted against the EGFR protein (PDB ID: 5UGB) to investigate their potential as anticancer leads. The results supported the *in silico* profile and revealed that compound **7** showed the most favorable predicted binding, and both compounds demonstrated binding patterns and affinities comparable to those of the reference drug.

In this work, suitable single crystals for compound 7 could not be obtained, and future studies will focus on structural optimization to improve solubility and on biological activity testing to confirm the activity of these compounds.

Acknowledgements

The authors extend their appreciation to the Deanship of Research and Graduate Studies at King Khalid University for funding this work through a Large Research Project under grant number RGP2/733/46.

Availability of data and materials

All data generated or analyzed during this study are included in this published article and its supplementary information files.

CRediT authorship contribution statement

Abdullatif Bin Muhsinah: Writing – review & editing, Methodology, Investigation, Funding acquisition, Data curation, Conceptualization. **Nabila A. Kheder:** Writing – review & editing, Writing – original draft, Validation, Investigation, Formal analysis, Data curation. **Ismail A. Elhaty:** Writing – review & editing, Writing – original draft, Validation, Software, Investigation, Formal analysis, Data curation. **Naglaa S. Mahmoud:** Writing – review & editing, Writing – original draft, Software, Formal analysis, Data curation. **Yahia N. Mabkhot:** Writing – review & editing, Validation, Supervision, Methodology, Investigation,

Data curation, Conceptualization.

Declaration of competing interest

The authors declare that they have no known competing financial interests or personal relationships that could have appeared to influence the work reported in this paper.

Supplementary materials

Supplementary material associated with this article can be found, in the online version, at doi:10.1016/j.molstruc.2026.146312.

Data availability

Data will be made available on request.

References

[1] B. Mathew, J. Suresh, S. Anbazhagan, Synthesis, in silico preclinical evaluation, antidepressant potential of 5-substituted phenyl-3-(thiophen-2-yl)-4,5-dihydro-1h-pyrazole-1-carboxamides, Biomed. Aging Pathol. 4 (4) (2014) 327–333, https://doi.org/10.1016/j.biomag.2014.08.002.

[2] P.N. Sable, S. Ganguly, P.D. Chaudhari, An efficient one-pot three-component synthesis and antimicrobial evaluation of tetra substituted thiophene derivatives, Chin. Chem. Lett. 25 (7) (2014) 1099–1103, https://doi.org/10.1016/j.cclet.2014.03.044.

[3] P. Mishra, A. Middha, V. Saxena, A. Saxena, Synthesis and evaluation of anti-inflammatory activity of some cinnoline derivatives-4 (-2-amino-thiophene) cinnoline-3-carboxamide, Pharm. Biosci. J. (2016) 64–68, https://doi.org/10.20510/ukjpb/4/i3/108388.

[4] H.M. Ashour, O.G. Shaaban, O.H. Rizk, I.M. El-Ashmawy, Synthesis and biological evaluation of thieno [2′,3′:4,5]pyrimido[1,2-b][1,2,4]triazines and thieno[2,3-d][1,2,4]triazolo[1,5-a]pyrimidines as anti-inflammatory and analgesic agents, Eur. J. Med. Chem. 62 (2013) 341–351, https://doi.org/10.1016/j.ejmech.2012.12.003.

[5] R. Kulandasamy, A.V. Adhikari, J.P. Stables, A new class of anticonvulsants possessing 6Hz activity: 3,4-dialkyloxy thiophene bishydrazones, Eur. J. Med. Chem. 44 (11) (2009) 4376–4384, https://doi.org/10.1016/j.ejmech.2009.05.026.

[6] S.Pathania Archna, P.A. Chawla, Thiophene-based derivatives as anticancer agents: an overview on decade's work, Bioorg. Chem. 101 (2020) 104026, https://doi.org/10.1016/j.bioorg.2020.104026.

[7] B. Insuasty, A. Montoya, D. Becerra, J. Quiroga, R. Abonia, S. Robledo, I.D. Vélez, Y. Upegui, M. Nogueras, J. Cobo, Synthesis of novel analogs of 2-pyrazoline obtained from [(7-chloroquinolin-4-yl)amino]chalcones and hydrazine as potential antitumor and antimalarial agents, Eur. J. Med. Chem. 67 (2013) 252–262, https://doi.org/10.1016/j.ejmech.2013.06.049.

[8] R.K.C. Hansa, M.M.K. Khan, M.M. Frangie, D.F. Gilmore, R.S. Shelton, A. V. Savenka, A.G. Basnakian, S.L. Shuttleworth, M.S. Smeltzer, M.A. Alam, 4-4-(Anilinomethyl)-3-[4-(trifluoromethyl)phenyl]-1H-pyrazol-1-ylbenzoic acid derivatives as potent anti-gram-positive bacterial agents, Eur. J. Med. Chem. 219 (2021) 113402, https://doi.org/10.1016/j.ejmech.2021.113402.

[9] L. Ravindar, S.A. Hasbullah, K.P. Rakesh, N.I. Hassan, Pyrazole and pyrazoline derivatives as antimalarial agents: a key review, Eur. J. Pharm. Sci. 183 (2023) 106365, https://doi.org/10.1016/j.ejps.2022.106365.

[10] R.Surendra Kumar, I.A. Arif, A. Ahamed, A. Idhayadhulla, Anti-inflammatory and antimicrobial activities of novel pyrazole analogues, Saudi J. Biol. Sci. 23 (5) (2016) 614–620, https://doi.org/10.1016/j.sjbs.2015.07.005.

[11] W.M. Eldehna, M.A. Alkabbani, Z.M. Elsayed, K.M. Ibrahim, T.A. Majrashi, M. Elagawany, R. Salem, H.A. Abdel-Aziz, H.O. Tawfik, Identification of novel triazole–Pyrazole conjugates as potential anticonvulsant agents: synthesis and biological evaluations, ACS Chem. Neurosci. 16 (15) (2025) 3038–3050, https://doi.org/10.1021/acschemneuro.5c00392.

[12] A.R.I. Morsy, S.H. Mahmoud, N.M. Abou Shama, W. Arafa, G.A. Yousef, A. A. Khalil, S.K. Ramadan, Antiviral activity of pyrazole derivatives bearing a hydroxyquinoline scaffold against SARS-CoV-2, HCoV-229E, MERS-CoV, and IBV propagation, RSC Adv. 14 (38) (2024) 27935–27947, https://doi.org/10.1039/D4RA04728A.

[13] D. Becerra, J.-C. Castillo, Recent advances in the synthesis of anticancer pyrazole derivatives using microwave, ultrasound, and mechanochemical techniques, RSC Adv. 15 (9) (2025) 7018–7038, https://doi.org/10.1039/D4RA08866B.

[14] I.A. Elhaty, N.A. Kheder, A.B. Muhsinah, Y.N. Mabkhot, A convenient synthesis of ethyl 5-amino-3-thioxo-3H-1,2-dithiole-4-carboxylate: crystal structure, computational studies, anticancer activity, and drug-likeness evaluation, J. Mol. Struct. (2026) 145286, https://doi.org/10.1016/j.molstruc.2026.145286.

[15] A.B. Muhsinah, N.A. Kheder, S.M. Soliman, I.A. Elhaty, Y.N. Mabkhot, Ethyl 4-methyl-2-(phenylamino)thiophene-3-carboxylate: one-pot synthesis, structural characterization, computational studies, and antitumor activity, J. Mol. Struct. 1352 (2026) 144424, https://doi.org/10.1016/j.molstruc.2025.144424.

[16] Y.A.A. Mohammed, N.A. Kheder, M.S. Nafie, A.A. Abbas, K.M. Dawood, Synthesis of some new pyrimidine-based pyrene/benzochromene hybrids as EGFR kinase inhibitors in HCT-116 cancer cells through apoptosis, RSC Adv. 15 (37) (2025) 30683–30696, https://doi.org/10.1039/D5RA03611A.

[17] Y.A.A. Mohammed, A.A. Abbas, A.M. Fahim, M.S. Nafie, K.M. Dawood, N. A. Kheder, One-pot three-component synthesis, structural characterization, computational investigation, and anti-cancer evaluation of some novel benzo[g][1,3,5]oxadiazocine pyridine carboxamide hybrids, J. Mol. Struct. 1347 (2025) 143269, https://doi.org/10.1016/j.molstruc.2025.143269.

[18] N.A. Kheder, A.M. Fahim, N.S. Mahmoud, K.M. Dawood, Unreported Biginelli product with potent antifungal activity: synthesis, DFT insights, and docking simulation analysis, J. Mol. Struct. 1330 (2025) 141480, https://doi.org/10.1016/j.molstruc.2025.141480.

[19] A.B. Muhsinah, N.A. Kheder, S.M. Soliman, H.A. Ghabbour, I.A. Elhaty, N. S. Mahmoud, M.A.A. Mahmoud, Y.N. Mabkhot, Chemoselective synthesis, structural elucidation, antitumor activity, Hirshfeld surface, and Fukui functions analysis of new thiophene derivatives, J. Mol. Struct. 1343 (2025) 142826, https://doi.org/10.1016/j.molstruc.2025.142826.

[20] A.B. Muhsinah, M.M. Alharbi, N.A. Kheder, S.M. Soliman, H.A. Ghabbour, N. S. Mahmoud, I.A. Elhaty, Y.N. Mabkhot, New thiophene derivatives: chemoselective synthesis, antitumor effectiveness, structural characterization, DFT calculations, Hirshfeld surface, and Fukui function analysis, BMC Chem. 18 (1) (2024) 228, https://doi.org/10.1186/s13065-024-01346-5.

[21] G.M. Sheldrick, SHELXT - integrated space-group and crystal-structure determination, Acta. Crystallogr. Found. Adv. 71 (Pt 1) (2015) 3–8, https://doi.org/10.1107/s2053273314026370.

[22] G.M. Sheldrick, A short history of SHELX, acta crystallographica, Found. Crystallogr. 64 (Pt 1) (2008) 112–122, https://doi.org/10.1107/s0108767307043930.

[23] C.F. MacRae, I. Sovago, S.J. Cottrell, P.T.A. Galek, P. McCabe, E. Pidcock, M. Platings, G.P. Shields, J.S. Stevens, M. Towler, P.A. Wood, Mercury 4.0: from visualization to analysis, design and prediction, J. Appl. Crystallogr. 53 (2020) 226–235, https://doi.org/10.1107/S1600576719014092.

[24] J.J. McKinnon, D. Jayatilaka, M.A. Spackman, Towards quantitative analysis of intermolecular interactions with Hirshfeld surfaces, Chem. Commun. (37) (2007) 3814–3816, https://doi.org/10.1039/B704980C.

[25] M.J. Turner, J.J. McKinnon, S.K. Wolff, D.J.S. Grimwood, R. P, D. Jayatilaka, M. A. Spackman, Crystal Explorer 17 University of Western Australia, 2017.

[26] M.A. Spackman, D. Jayatilaka, Hirshfeld surface analysis, CrystEngComm 11 (1) (2009) 19–32, https://doi.org/10.1039/B818330A.

[27] A.D. Becke, Density-functional thermochemistry. III. The role of exact exchange, J. Chem. Phys. 98 (7) (1993) 5648–5652, https://doi.org/10.1063/1.464913.

[28] J.-I. Aihara, Reduced HOMO−LUMO gap as an index of kinetic stability for polycyclic aromatic hydrocarbons, J. Phys. Chem. A 103 (37) (1999) 7487–7495, https://doi.org/10.1021/jp990092i.

[29] S. Uzun, Z. Esen, E. Koç, N.C. Usta, M. Ceylan, Experimental and density functional theory (MEP, FMO, NLO, Fukui functions) and antibacterial activity studies on 2-amino-4- (4-nitrophenyl) -5,6-dihydrobenzo [h] quinoline-3-carbonitrile, J. Mol. Struct. 1178 (2019) 450–457, https://doi.org/10.1016/j.molstruc.2018.10.001.

[30] O. Trott, A.J. Olson, AutoDock Vina: improving the speed and accuracy of docking with a new scoring function, efficient optimization, and multithreading, J. Comput. Chem. 31 (2) (2010) 455–461, https://doi.org/10.1002/jcc.21334.

[31] T. Sander, J. Freyss, M. von Korff, J.R. Reich, C. Rufener, OSIRIS, an entirely in-house developed drug discovery informatics system, J. Chem. Inf. Model. 49 (2) (2009) 232–246, https://doi.org/10.1021/ci800305f.

[32] Ş. Çakmak, Z. Demircioğlu, S. Uzun, A. Veyisoğlu, H. Yakan, C.C. Ersanli, Synthesis, X-ray structure, antimicrobial activity, DFT and molecular docking studies of N-(thiophen-2-ylmethyl)thiophene-2-carboxamide, Acta Crystallogr. C Struct. Chem. 78 (Pt 7) (2022) 390–397, https://doi.org/10.1107/s2053229622006283.

[33] G. Khanum, A. Fatima, N. Siddiqui, D.D. Agarwal, R.J. Butcher, S.K. Srivastava, S. Javed, Synthesis, single crystal, characterization and computational study of 2-amino-N-cyclopropyl-5-ethyl-thiophene-3-carboxamide, J. Mol. Struct. 1250 (2022) 131890, https://doi.org/10.1016/j.molstruc.2021.131890.

[34] N.A. Ancın, S.G. Öztaş, Ö. Küçükterzi, N.A. Öztaş, Theoretical investigation of N-trans-cinnamylidene-m-toluidine by DFT method and molecular docking studies, J. Mol. Struct. 1198 (2019) 126868, https://doi.org/10.1016/j.molstruc.2019.07.115.

[35] I.A. Elhaty, N.A. Kheder, A.B. Muhsinah, Y.N. Mabkhot, A convenient synthesis of ethyl 5-amino-3-thioxo-3H-1,2-dithiole-4-carboxylate: crystal structure, computational studies, anticancer activity, and drug-likeness evaluation, J. Mol. Struct. 1358 (2026) 145286, https://doi.org/10.1016/j.molstruc.2026.145286.

[36] N.A. Kheder, S. Tasqeeruddin, N.S. Mahmoud, M.A.A. Mahmoud, I.A. Elhaty, One-pot synthesis of new bis(2,4′-bipyridine), bis(pyrrole), and bis(benzo[f]chromene) derivatives: antimicrobial evaluation, molecular docking, DFT, and ADME profiling, J. Mol. Struct. (2025) 144065, https://doi.org/10.1016/j.molstruc.2025.144065.

[37] H.E.N. Khasawneh, H.M. Hassan, A.A. Alharbi, W.T. Almagharbeh, R.F.A. Al-Aouadi, K. Kaur, R. Maranan, H.M. Farhan, H. Hashem, M.M. Hassan, S. Bräse, A. Al-Emam, Current progress of 1,2,3-triazole hybrids as EGFR inhibitors for cancer therapy – a literature review, RSC Adv. 15 (48) (2025) 40998–41047, https://doi.org/10.1039/D5RA03819G.

[38] T. Amelia, R.E. Kartasasmita, T. Ohwada, D.H. Tjahjono, Structural insight and development of EGFR tyrosine kinase inhibitors, Molecules 27 (3) (2022), https://doi.org/10.3390/molecules27030819.

[39] M.N. Sallam, A.A. Al-Karmalawy, E.M. Abbass, S.S. Hawas, A.M. El-Naggar, A.M. A. Hassan, Design, synthesis, and anticancer evaluation of novel pyrazole–thiophene hybrid derivatives as multitarget inhibitors of wild EGFR, mutant (T790M) EGFR, and VEGFR-2, RSC Adv. 15 (47) (2025) 40078–40092, https://doi.org/10.1039/d5ra06852e.

[40] H.I. Gul, C. Yamali, H. Sakagami, A. Angeli, J. Leitans, A. Kazaks, K. Tars, D. O. Ozgun, C.T. Supuran, New anticancer drug candidates sulfonamides as selective hCA IX or hCA XII inhibitors, Bioorg., Chem. 77 (2018) 411–419, https://doi.org/10.1016/j.bioorg.2018.01.021.

[41] S. Samy, S.E. Mahmoud, E. Abdel-Galil, E. Abdel-Latif, G.E. Said, Development of new pyrazole–thiophene hybrids: synthesis, anticancer assessment, and molecular docking insights, RSC Adv. 16 (12) (2026) 10665–10678, https://doi.org/10.1039/D6RA00429F.

[42] G.M. Cooper, The cell: a molecular approach. Sunderland (ma) sinauer associates, Struct. Organ. Actin Filam. (2000).